

Supplementary Information

Tandem electrocatalytic N₂ fixation via concerted proton-electron transfer

Pablo Garrido-Barros, Joseph Derosa, Matthew J. Chalkley and Jonas C. Peters*

*Corresponding author. Email: jpeters@caltech.edu

Table of Contents:

3-7	S1. General Materials and Methods
8-14	S2. Ammonia quantification
15-17	S3. Electrocatalysis using $\mathbf{W}(\text{N}_2)_2$ under original conditions
18-23	S4. Optimization of N_2RR conditions using $\mathbf{W}(\text{N}_2)_2$
24-34	S5. Control experiments for electrocatalytic N_2RR
35-37	S6. Protonation of $\mathbf{W}(\text{N}_2)_2$
38-40	S7. Mechanistic analysis via Cyclic Voltammetry
41-47	S8. Chemical CPET reactions
48-58	S9. Electrochemical analysis of N_2RR catalysts
59-60	S10. References

S1. General Materials and Methods:

S1.1. General Considerations:

All manipulations were carried out using standard Schlenk or glovebox techniques under an N₂ or Ar atmosphere as specified. Solvents were deoxygenated and dried by thoroughly sparging with N₂ followed by passage through an activated alumina column in a solvent purification system by SG Water, USA LLC. Subsequently, the solvents were further dried and stored under N₂ atmosphere inside a glove box with molecular sieves obtained from Sigma Aldrich that were activated at 200°C overnight under vacuum. Non-halogenated solvents were tested with sodium benzophenone ketyl in tetrahydrofuran (THF) in order to confirm the absence of oxygen and water. Deuterated d₆-DMSO solvent (D, 99.9% with a purity of 99.5%) was purchased from Cambridge Isotope Laboratories, Inc., and use as received. Isotope labelled ¹⁵N₂ gas cylinder was purchased from Cambridge Isotope Laboratories, Inc., NLM-363-1-LB, PSO #:21A-0223, Lot #: I-24583/A R0664758.

N₂ gas in a NEXUS glovebox (Vacuum Atmospheres Company) was purified by a Nexus modular purification system. The purity of N₂ gas was assessed via colorimetric, gas chromatography and NMR methods, with regard to NH₃, N₂O, NO₂⁻ and NO₃⁻ impurities, as detailed in further sections.

Cobaltocenium hexafluorophosphate ([Cp₂Co][PF₆]), triflic acid, ferrocene, silver triflate, tetrabutylammonium tetrafluoroborate ([TBA][BF₄]; TBA = tetra-*N*-butylammonium), lithium perchlorate ([Li][ClO₄]), tosic acid (TsOH) were all used as purchased from Sigma Aldrich. [Li][OTf] (OTf = trifluoromethanesulfonate) and [Li][NTf₂] (NTf₂ = bis(trifluoromethanesulfonyl)imide) were also obtained from Sigma Aldrich and further dried under vacuum at 100 °C for 120 h prior use. Tetrabutylammonium hexafluorophosphate ([TBA][PF₆]) from Sigma Aldrich was recrystallized from ethanol prior to use. Silver triflate (AgOTf) was purchased from Strem and used without further purification. The absence of any detectable NH₄⁺, NO₃⁻ or NO₂⁻ impurities in the electrolyte solution coming from either solvent, electrolyte or acid was analyzed by subjecting the solutions to NH₄⁺ detection via ¹H-NMR spectroscopy and NO₂⁻/NO₃⁻ detection via the Griess method (*vide infra*). Whenever water was specified as solvent, deionized water OmniSolv (Supelco, Sigma Aldrich) was used to prepare the solutions.

* Cited literature for the preparation of known inorganic compounds:

(Cp)Co(Cp^N),¹ [(Cp)Co(Cp^N)] [OTf],¹ [(Cp)Co(Cp^{NH})] [OTf]₂,¹ [(dppe)₂W(N₂)₂],² [(dppe)₂W(NNH₂)(OTs)],³ [(dppe)₂W(N)(N₃)],⁴ [(dppe)₂Mo(N₂)₂],² [(PPh₂Me)₄Mo(N₂)₂],⁵ [Mo(N₂)₂(PNP)]₂(μ-N₂),⁶ [Mo(I)₃(PNP)],⁷ (P₃Si)Os(N₂),⁸ [(P₃B)Fe]⁺,⁹ (P₃Si)Fe(N₂),¹⁰ [Na][BAR^F₄] (BAR^F₄ = B(3,5-(CF₃)₂-C₆H₃)₄),¹¹ and TsOD¹² were synthesized as described previously.

S1.2 Griess method reagents:

Reagents for the Griess method for NO₂⁻ quantification were purchased from Sigma Aldrich and include: sulphanilamide, HCl solution (32 wt.%), and N-1-naphthylethylenediamine dihydrochloride. Two solutions were prepared for the colorimetric method according to the literature procedure¹³: the first one containing 0.1 g of sulphanilamide in 1 mL HCl solution, adjusting the final volume to 10 mL with deionized water; the second contains 10 mg of N-1-

naphthylthylenediamine dihydrochloride in 10 mL of deionized water. Both solutions were stored in amber bottle and refrigerated. For NO_3^- quantification, a solution containing 0.02 wt.% VCl_3 in 6 M HCl was also employed to quantitatively reduce NO_3^- to NO_2^- .

S1.3 NMR Spectroscopy:

^1H -NMR spectra were recorded with a Varian 400 MHz spectrometer and chemical shifts are reported in ppm relative to tetramethylsilane, using ^1H resonances from residual solvent as internal standards. ^{31}P NMR spectra were also recorded with Varian 400 MHz and referenced to the H_3PO_4 signal.

For detection of NH_4^+ , 1,3,5-trimethoxybenzene was employed as an internal standard, purchased from Sigma Aldrich and used as received; a solution of 8 M H_2SO_4 (98%, Thermo Fischer Scientific) in d_6 -DMSO was employed to control the final pH of the NMR sample.¹⁴

S1.4 UV-vis Spectroscopy:

Measurements were taken on a Cary 50 UV-visible spectrophotometer using a 1 cm quartz cell sealed with a Teflon stopcock.

S1.5 Gas chromatography:

Gas chromatography coupled to a thermal conductivity detector (GC-TCD) was employed to detect for possible contamination of N_2O in the $^{14}\text{N}_2$ and $^{15}\text{N}_2$ gas supply. A 100 μL Hamilton syringe was used to sample the headspace and to inject into the GC-TCD. GC-TCD was performed in the Environmental Analysis Center (Caltech) using a HP 5890 Series II instrument with Helium as the carrier gas. Calibration was determined by direct injection of known volumes of N_2O .

S1.6 Electrochemistry:

A CHI instruments 600B and a Biologic VSP potentiostat were used for all electrochemical data collection.

Cyclic voltammetry (CV), linear sweep voltammetry (LSV) and differential pulse voltammetry (DPV) experiments were carried out in a one-compartment three-electrode cell using a boron doped diamond (BDD) disk as the working electrode (3 mm diameter), a Pt disk as the counter electrode, and an Ag/AgOTf (5 mM) reference electrode. Details for the CVs and LSVs are noted as they appear. DPVs were obtained with the following parameters: amplitude = 50 mV, step height = 4 mV, pulse width = 0.05 s, pulse period = 0.5 s and sampling width = 0.0167 s. $E_{1/2}$ values for the reversible waves were obtained from the half potential between the oxidative and reductive peaks and, for irreversible processes, were estimated according to the potential at the i_{max} in DPV measurements. For all measurements IR compensation was applied accounting for 85% of the total resistance. All the reported potentials are referenced to the ferrocenium/ferrocene couple ($\text{Fc}^{+/0}$) used as an external standard.

Controlled potential coulometries (CPCs) were carried out in a gas-tight, two-compartment or H-cell equipped with a frit to separate anodic from cathodic chambers (Fig. S1). This cell also features two necks, one in each compartment, sealed using a septum that allows for bubbling of different gasses other than the $^{14}\text{N}_2$, such as Argon and $^{15}\text{N}_2$, needed in control experiments. Either a BDD plate (dimensions 1x1 cm) or a high surface area reticulated vitreous carbon foam was employed as the working electrode, a Ag/AgOTf (5 mM) as the reference electrode, and a Zn plate

as the sacrificial counter electrode. In a typical experiment, 6 mL of solvent containing 0.2-0.1 M of the specified electrolyte and the toxic acid was added to the electrochemical cell, 3 mL per compartment. For experiments including the catalysts, the cathodic chamber was also charged with the corresponding amount of Co(III,N)^+ mediator and $\text{W(N}_2)_2$ (or other N_2RR catalyst), or both were taken from concentrated stock solutions (1 mg/mL). The electrochemical cell was assembled inside an N_2 glove box in which the CPC experiment was also performed. The potential applied during the CPC experiment was set to $-1.35\text{ V vs Fc}^{+/0}$ according to the peak current observed for the catalytic wave from previous CVs. The solution was stirred throughout the CPC experiment.

The BDD disk electrode for cyclic voltammetry was polished using a PK-3 polishing kit with $6\text{ }\mu\text{m}$ diamond (Biologic). The BDD plate electrodes were pre-treated according to literature procedures.¹⁵ The Zn counter electrode was polished with a stainless steel sponge, washed repeatedly with water and acetone and vacuum dried.

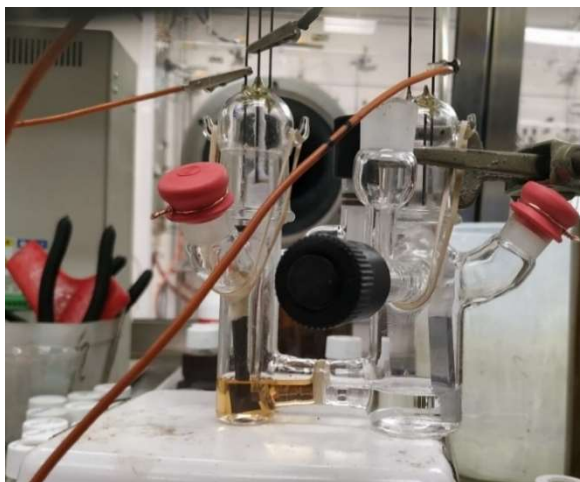


Fig. S1. Gas-tight, two-compartment electrochemical cell set up employed in the CPC experiments. It is composed of two Kontes valves, two 14/24 necks closed by septa fastened with copper-wire, and two 24/40 necks for the incorporation of the electrodes that are connected to the potentiostat leads via crossing tungsten wires.

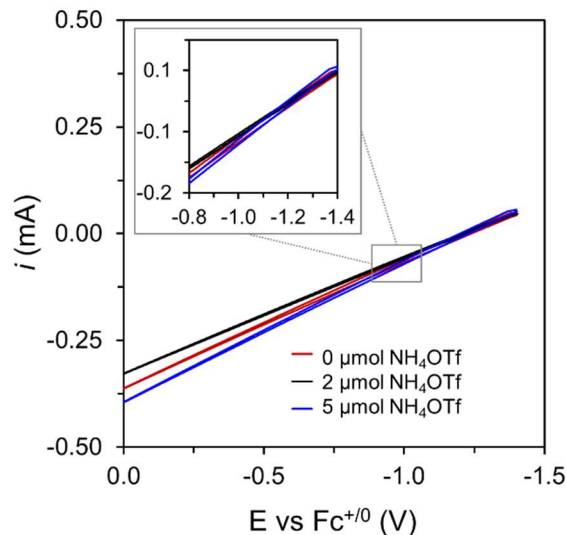


Fig. S2. CV of the Zn electrode employed as sacrificial counter electrode in the CPC experiments in 0.2 M [TBA][BF₄] THF solution containing different concentrations of NH₄OTf and 50 mM TsOH, using a GC plate counter electrode.

S1.7 Kinetic analysis from cyclic voltammetry:

For kinetic analysis via cyclic voltammetry, a multielectron/multiproton electrocatalytic process can be simplified to an EC_{cat} mechanism involving an electrode-mediated electron transfer process (E) coupled to a catalytic chemical reaction (C_{cat}), which will reflect a convolution of the elementary chemical steps of catalysis.¹⁶ For an EC_{cat} process under pure kinetic conditions, an ideal S-shape response would be obtained featuring a current intensity in the catalytic plateau (i_{cat}) described by **Eq. S1**. In this equation, n_e is the number of electrons involved in the catalytic cycle, F is the Faraday constant, S is the area of the electrode, D_{cat} is the diffusion coefficient of the catalyst and k_{obs} is the observed kinetic constant of the catalytic process which will reflect a convolution of the kinetically relevant steps of catalysis and will follow a mathematical expression depending on the rate law. Therefore, the intensity of the catalytic plateau should increase linearly with the concentration of the catalysts, C_{cat}^0 , and with the square root of k_{obs} that in turns incorporate the concentration of the substrates involved in the rate determining steps.

$$i_{cat} = n_e F S C_{cat}^0 \sqrt{D_{cat}} \sqrt{k_{obs}} \quad (\text{Eq. S1})$$

In the present case of tandem catalysis, each of the coupled catalytic cycles (CPET and N₂RR) will provide a catalytic current according to **Eq. S1** that will depend on their specific mechanism. Although the multielectron/multiproton character of this overall process and the interplay between both catalytic cycles complicate obtaining an exact analytical solution, the overall observed current will be a convolution of the current for each of the catalytic cycles.

For a proposed mechanism where the mediator reduces certain intermediates of the N₂RR cycle via a rate determining CPET, with the rest of electron transfers happening at the electrode, the expression for the catalytic current due to CPET is going to depend linearly on the concentration of the mediator ([Co]) and on the square root of the **W** catalyst concentration ([W]), **Eq. S3**. At the same time, the catalytic current associated to the N₂RR cycle, assuming that the

intermediates can be reduced by the CPET mediator or directly at the electrode followed by further protonation TsOH in solution, the observed catalytic current will increase linearly with $[W]$ and with $k_{obs}(N_2RR)^{1/2}$, **Eq. S4**, which in turn will have a positive dependence on $[Co]$ due to a rate limiting CPET, and possibly on $[TsOH]$, according to the relative rate of protonation steps, **Eq. S5**.

$$i_{obs} = i_{cat}(CPET) + i_{cat}(N_2RR) \quad (\text{Eq. S2})$$

$$i_{cat}(CPET) = FS[Co]\sqrt{D_{Co}}\sqrt{k_{CPET}[W]} \quad (\text{Eq. S3})$$

$$i_{cat}(N_2RR) = n_eFS[W]\sqrt{D_{Co}}\sqrt{k_{obs}(N_2RR)} \quad (\text{Eq. S4})$$

$$k_{obs}(N_2RR) = f([Co], [TsOH]) \quad (\text{Eq. S5})$$

In order to obtain preliminary information about the rate law for the tandem catalytic process and support our proposals, we have examined how changes in the concentration of the different components affect the behavior of the i_{cat} during CV experiments. Herein, we are evaluating i_{cat} as the maximum current of the electrocatalytic wave obtained from background corrected CVs as its behavior approached the S-shape expected from an ideal electrocatalytic response in the pure kinetic regime (*vide infra*).

The kinetic isotope effect, *KIE*, can be determined by evaluating k_{obs} for the reaction in the presence of protio-acid, TsOH, and deuterio-acid, TsOD and comparing them as in **Eq. S6**. As aforementioned, the complications in obtaining the mathematical expression for this tandem electrocatalytic system preclude calculation of meaningful k_{obs} values. However, as deduced from **Eq. S1**, i_{cat} is proportional to the square root of k_{obs} for a simplified EC_{cat} mechanism describing our more complex system, so we have estimated a value for *KIE* from the ratio between the i_{cat} values observed in the presence of each acid.

$$KIE = \frac{k_{obs} (^1H)}{k_{obs} (^2H)} = \frac{[i_{cat} (^1H)]^2}{[i_{cat} (^2H)]^2} \quad (\text{Eq. S6})$$

S2. Ammonia quantification:

S2.1 General work-up procedure:

Upon completion of CPC experiments, excess of acid (twice as much as the theoretical amount of ammonia produced) was added through the septum with a syringe in order to quench all possible free ammonia in solution as NH_4^+ . Subsequently, the cell was placed in a cold well at $-78\text{ }^\circ\text{C}$ using a dry ice/acetone bath in order to condense possible evaporated ammonia in the headspace. After 10 min at this temperature, the electrochemical cell was brought to room temperature and allowed to stir for another 10 min in the presence of the excess acid. The solution was then transferred with a pipette into a Schlenk tube; the cell was subsequently washed with more solvent that was also collected into the same tube. The tube was tightly sealed with a Kontes cap, brought out of the glove box and placed into liquid N_2 allowing 10 min for the entire solution to freeze. Once frozen, the Schlenk tube was opened and 2 equivalents of sodium *tert*-butoxide (NaO^tBu_4) base per mol of total acid (initial acid loading plus quenching acid) were slowly delivered in the form of a 2.5 M MeOH solution, leaving 5 min at liquid nitrogen temperature for equilibration. Afterwards, the headspace of the tube was evacuated to constant pressure and the tube was closed and brought to room temperature, stirring for 10 min to react all the NH_4^+ with the added base to liberate NH_3 . At the same time, in a different tube, 2 mL of a 2.0 M HCl solution in diethyl ether was prepared. In the next step the NH_3 solution was vacuum transferred to the ethereal HCl solution to remove non-volatile components of the reaction mixture, including the catalysts, the electrolyte, the resulting sodium tosylate (NaOTs) and the excess of NaO^tBu_4 . The resultant solution (NH_3 and ethereal HCl) was allowed to react for 10 min at room temperature and then evaporated to dryness, affording NH_4Cl . The latter was extracted with 0.5 mL of 1 mM 1,3,4-trimethoxybenzene (TMB) in d_6 -DMSO for ^1H -NMR analysis. Analysis of the total amount of NH_3 produced after isolation via vacuum transfer overcomes some of the challenges associated with low ammonia concentrations or interferences of the electrolyte solution in the quantification methods when direct sampling from the electrolyte solution is employed for the analysis.¹⁷ Moreover, the amounts of NH_3 produced in the present work are well above those of background levels (section S6). Nonetheless, appropriate control experiments have been carried out in order to verify the source of the generated NH_3 as a result of electrocatalytic N_2RR (section S6).

S2.2 ^1H -NMR quantification:

Sample preparation for quantification via ^1H -NMR methods involves extracting the solid NH_4Cl after work up with 0.5 mL of 1 mM TMB in d_6 -DMSO. To this solution, 10 μL of 8 M H_2SO_4 solution in d_6 -DMSO were added (0.2 M final concentration) to ensure constant acidic conditions of the resulting sample and minimize variations due to different proton activities of the resulting sample.^{14,18}

Despite its high selectivity for NH_4^+ detection, ^1H -NMR spectroscopy has proven to be challenging for accurate quantification due to the interplay between d_1 , T_1 and the proton exchange-induced loss of coherence in determining the intensity of the NMR peak, and their different response to changes in the sample concentration and proton concentration.¹⁴ This can cause absolute, quantitative NMR (qNMR), based on direct integration with respect to an internal standard with a known concentration, frequently result in over- or underestimation of the total NH_4^+ .¹⁸ Therefore, ^1H -NMR analysis of NH_4^+ via relative quantification using a calibration curve and an internal standard is preferred as a reliable method for fast determination.

We have employed this method using TMB as an internal standard. In order to obtain a calibration curve, a stock solution of NH₄Cl (1mg/mL) in 1 mM TMB in d₆-DMSO solution was prepared. From that stock solution, different volume aliquots were diluted with the same 1 mM TMB in d₆-DMSO solution up to a total volume of 0.5 mL, resulting in standard samples with differing concentrations of NH₄Cl. To each of those solutions, 10 μL of 8 M H₂SO₄ in d₆-DMSO were added to obtain a constant and controlled proton concentration in the final sample, preventing possible errors in the calibration associated with different degrees of acidity in different samples. ¹H-NMR spectra of these standard samples afforded the calibration curve via integration of the 4 protons of the NH₄⁺ peak (N_{NH₄⁺}) in the range 7.3-6.9 ppm relative to the 3 aryl protons of TMB (N_{TMB}) at around 6.1 ppm according to **Eq. S7**, where I, C, and N are the integral, concentration and number of protons respectively for each component.

$$C_{NH_4^+} = \frac{I_{NH_4^+} N_{TMB}}{I_{TMB} N_{NH_4^+}} C_{TMB} \quad (\text{Eq. S7})$$

¹H-NMR spectra obtained from the standard samples are shown in Fig. S3 and S5 and resulting calibration plots are shown in Fig. S4 and S6. Two calibration plots were prepared using two different concentrations of internal standard (TMB) of 1 mM and 5 mM respectively. A similar procedure was followed to prepare the calibration plot for ¹⁵NH₄⁺ used in the ¹⁵N₂ labelled experiments, and the results are shown in Fig. S7 and S8. In both cases, a reliable linear fit was obtained with R² > 0.99.

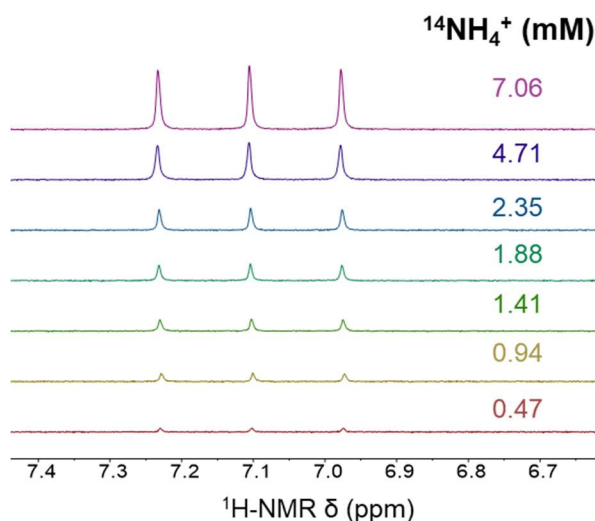


Fig. S3. ¹H-NMR spectra of standard samples containing different concentrations of NH₄Cl in 1mM TMB d₆-DMSO solution.

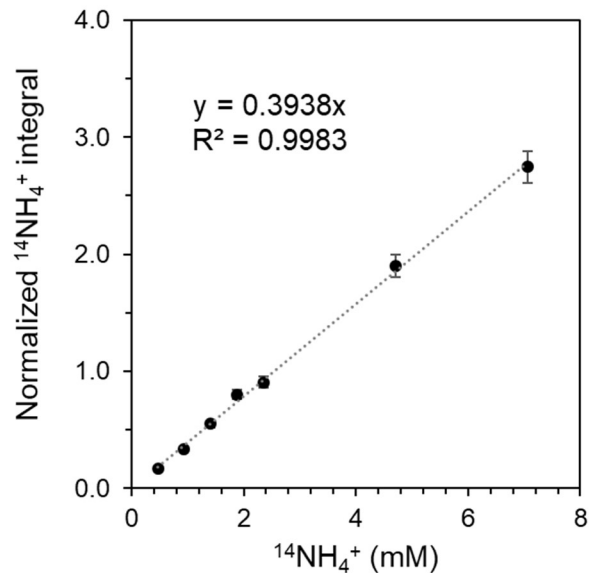


Fig. S4. Calibration curve according to **Eq. S7** for the ^1H -NMR spectra of standard $^{14}\text{NH}_4\text{Cl}$ samples presented in Fig. S3. The normalized integral was obtained by integration of the triplet in the 7.3-6.9 ppm region corresponding to the 4 protons of $^{14}\text{NH}_4^+$ relative to the integration of the singlet at 6.1 ppm corresponding to the 3 aryl protons of TMB (1 mM concentration). For each concentration point, an average of 3 independent measurements is shown together with the error bars.

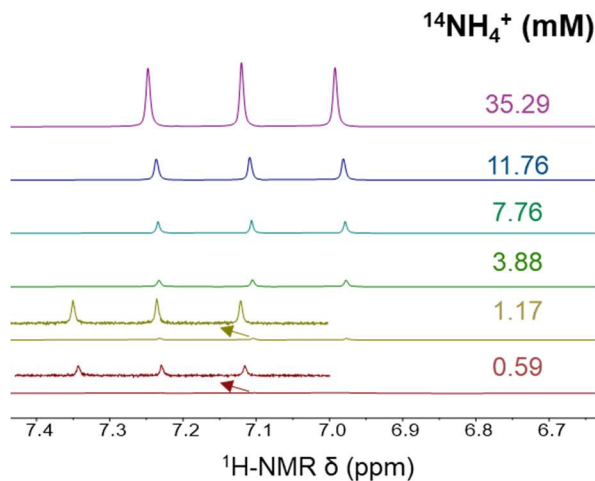


Fig. S5. ^1H -NMR spectra of standard samples containing different concentrations of NH_4Cl in 5mM TMB d_6 -DMSO solution. For the spectra of 1.17 and 0.59 mM NH_4Cl , a magnification of the NH_4^+ peaks is included.

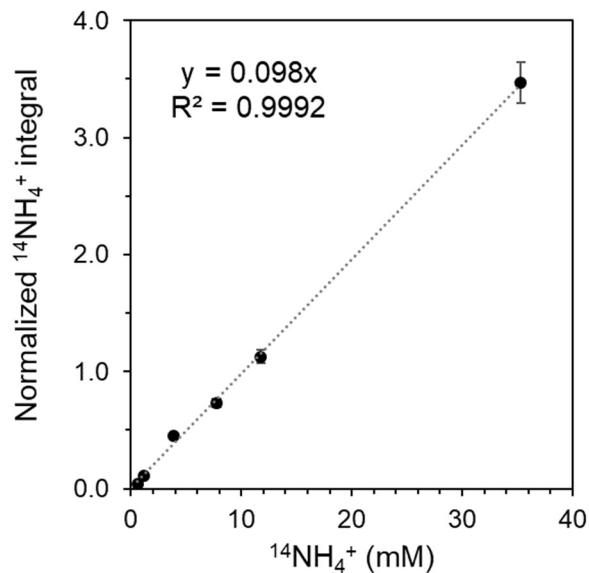


Fig. S6. Calibration curve according to **Eq. S7** for the ^1H -NMR spectra of standard $^{14}\text{NH}_4\text{Cl}$ samples presented in Fig. S5. The normalized integral was obtained by integration of the triplet in the 7.3-6.9 ppm region corresponding to the 4 protons of $^{14}\text{NH}_4^+$ relative to the integration of the singlet at 6.1 ppm corresponding to 3 aryl protons of TMB (5 mM concentration). For each concentration point, an average of 3 independent measurements is shown together with the error bars.

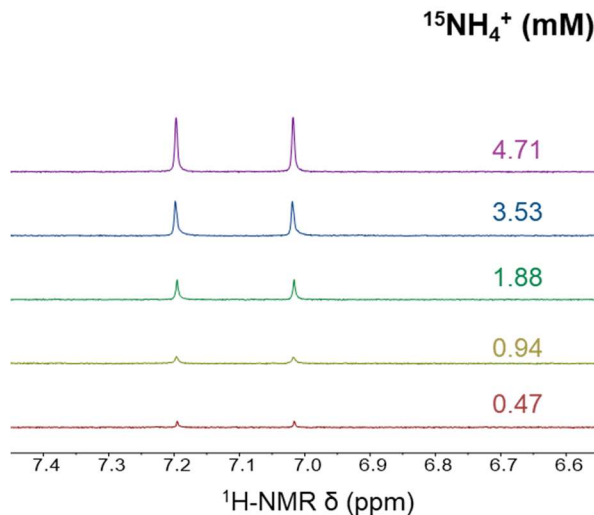


Fig. S7. ^1H -NMR spectra of standard samples containing different concentrations of $^{15}\text{NH}_4\text{Cl}$ in 1mM TMB d_6 -DMSO solution.

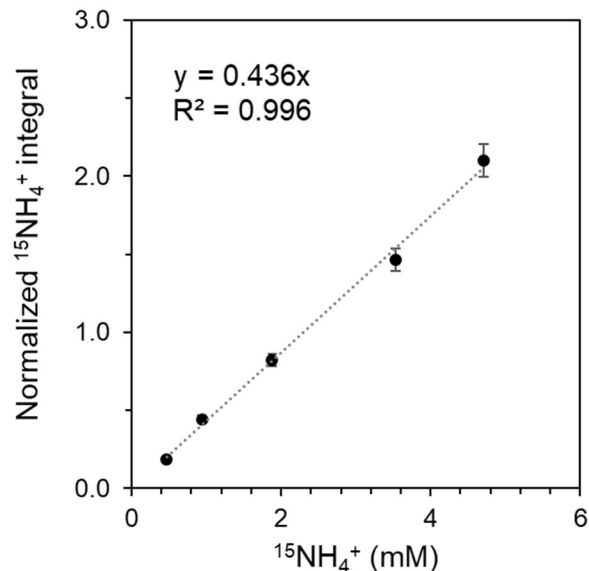


Fig. S8. Calibration curve according to **Eq. S7** for the ^1H -NMR spectra of standard $^{15}\text{NH}_4\text{Cl}$ samples presented in Fig. S7. The normalized integral was obtained by integration of the doublet in the 7.3-6.9 ppm region corresponding to the 4 protons of $^{15}\text{NH}_4^+$ relative to the integration of the singlet at 6.1 ppm corresponding to 3 aryl protons of TMB (1 mM concentration). For each concentration point, an average of 3 independent measurements is shown together with the error bars.

Several methodologies have also been reported to minimize issues associated with absolute NH_4^+ quantification via an internal standard, which consider variables from sample preparation to internal standard selection and specific ^1H -NMR sequences in order to improve the accuracy and detection limit. One promising approach is based on selective excitation of protons from the NH_4^+ , as reported by Jaramillo and coworkers.¹⁷ They employ the Frequency-Selective pulse Gradient Spin Echo (selgspe) sequence that selectively excite the protons with NMR signals in a small region centered where the NH_4^+ appear (~ 7.1 ppm). While this method still involves longer acquisition times than the NMR method described previously based on calibration plots, it minimizes the proton solvent signals as one of the primary challenges for NH_4^+ detection and generates strong NH_4^+ signals, thereby providing one of the highest sensitivities for quantitation. The concentration of NH_4Cl was determined by integration of the area below the NH_4^+ peaks compared to that of the internal standard. We employed TMB which is compatible for quantification via both previous calibration plots and this selective excitation method as shown in Fig. S9 due to the proximity of the three aryl peaks of TMB to the NH_4^+ region. Calculation of the concentration of standard samples of NH_4Cl was performed by both direct quantitative integrations relative to the internal standard (Fig. S11) and by generation of a calibration plot (Fig. S10). As evidenced by the results, this method offers a means for both absolute quantification via direct comparison to the internal standard peak added in known concentration and quantification by the use of the calibration curve. Results from application of this method were consistent with those obtained from the previous approach.

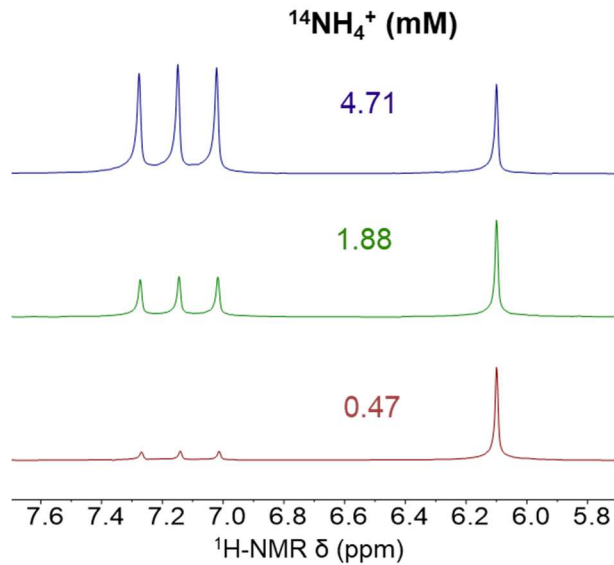


Fig. S9. ^1H -NMR spectra of standard samples containing different concentrations of NH_4Cl in 1mM TMB d_6 -DMSO solutions using Frequency-Selective pulse Gradient Spin Echo.

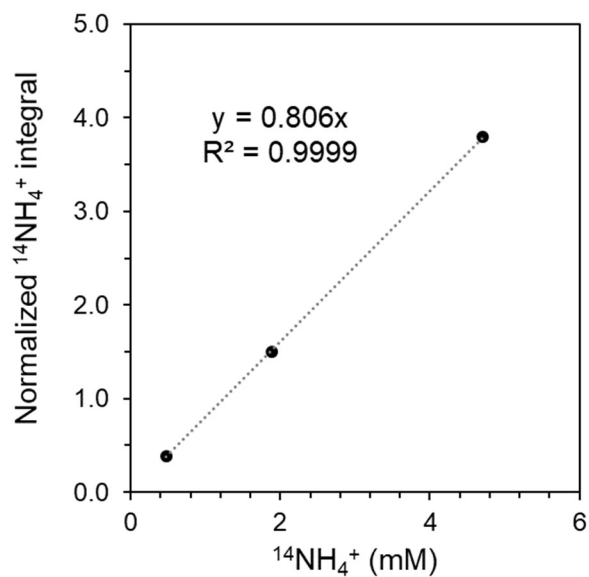


Fig. S10. Calibration curve according to Eq. S7 for the ^1H -NMR spectra of standard $^{14}\text{NH}_4\text{Cl}$ samples presented in Fig. S9. The normalized integral was obtained by integration of the triplet in the 7.3-6.9 ppm region corresponding to the 4 protons of $^{14}\text{NH}_4^+$ relative to the integration of the singlet at 6.1 ppm corresponding to 3 aryl protons of TMB (1 mM concentration).

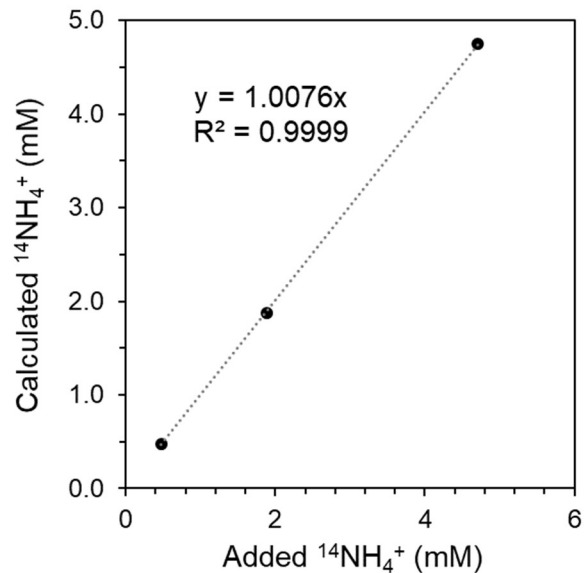


Fig. S11. Plot of the calculated NH_4^+ amount via absolute quantification with internal standard versus the amount of NH_4Cl added to the sample. The high correlation with $R^2 > 0.99$ reflects the adequacy of this method for direct quantitative NMR determination of NH_4^+ .

S2.3 Faradaic Efficiency:

The Faradaic efficiency (FE) was calculated considering the total charge passed during the CPC experiments (Q), the number of electrons involved in the formation of one molecule of NH_3 ($n_e = 3$), the Faraday constant (F) and the mols of NH_3 produced (N_{NH_3}), following **Eq. 8**:

$$FE = \frac{N_{\text{NH}_3}}{\frac{Q}{n_e F}} \quad (\text{Eq. 8})$$

S3. Electrocatalysis using $\mathbf{W(N_2)_2}$ under original conditions

As reported by Becker and coworkers,² previous attempts experiments to render the $\mathbf{W(N_2)_2}$ system electrocatalytic for $\mathbf{N_2RR}$ by CPC in the presence of acid employed glassy carbon as a working electrode, among other electrodes, THF as solvent, $[\mathbf{TBA}][\mathbf{BF_4}]$ as electrolyte (TBA = tetra-*N*-butylammonium) and tosic acid (TsOH) as proton source. We performed control electrocatalytic experiments using related conditions so as to compare results from the tandem CPET- $\mathbf{N_2RR}$ approach presented in this work, with these previous approaches.

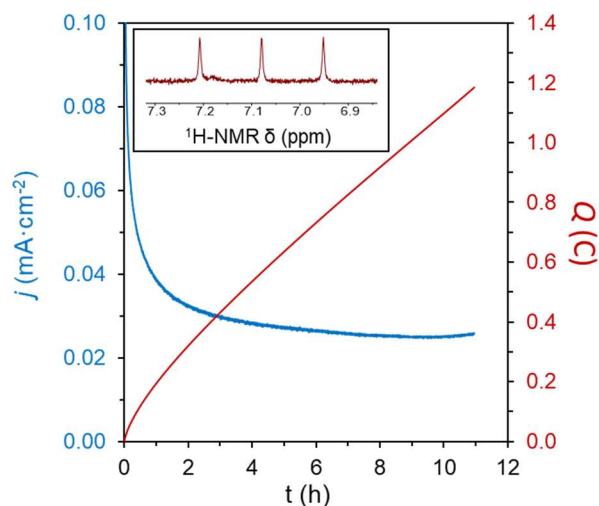


Fig. S12. Current and charge profile for a CPC at -1.35 V vs $\mathbf{Fc}^{+/0}$ in 0.2 M $[\mathbf{TBA}][\mathbf{BF_4}]$ THF solution containing 0.05 mM $\mathbf{Co(III,N)^+}$, 0.05 mM $\mathbf{W(N_2)_2}$ and 5 mM TsOH, using a GC plate working electrode. **Inset:** Quantification of generated $\mathbf{NH_3}$ via $^1\mathbf{H-NMR}$ spectroscopy.

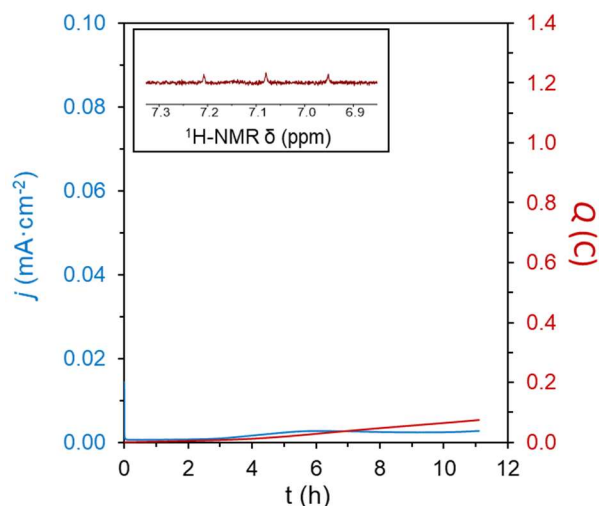


Fig. S13. Current and charge profile for a CPC at -1.35 V vs $\mathbf{Fc}^{+/0}$ in 0.2 M $[\mathbf{TBA}][\mathbf{BF_4}]$ THF solution containing 0.05 mM $\mathbf{W(N_2)_2}$ and 5 mM TsOH, using a GC plate working electrode. **Inset:** Quantification of generated $\mathbf{NH_3}$ via $^1\mathbf{H-NMR}$ spectroscopy.

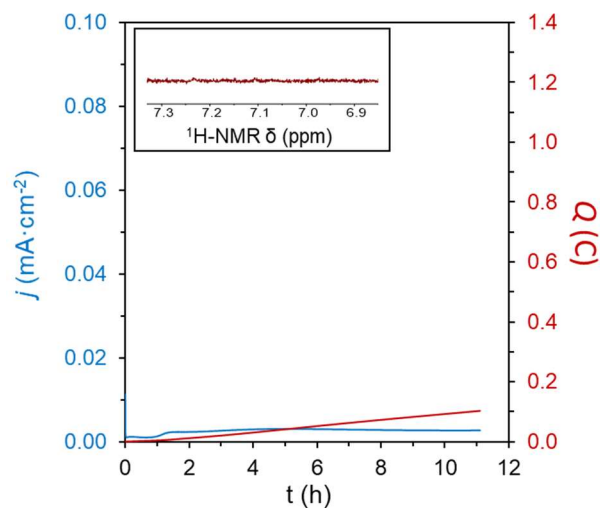


Fig. S14. Current and charge profile for a CPC at -1.35 V vs $\text{Fc}^{+/0}$ in 0.2 M $[\text{TBA}][\text{BF}_4]$ THF solution containing and 5 mM TsOH, using a GC plate working electrode. **Inset:** Quantification of generated NH_3 via $^1\text{H-NMR}$ spectroscopy.

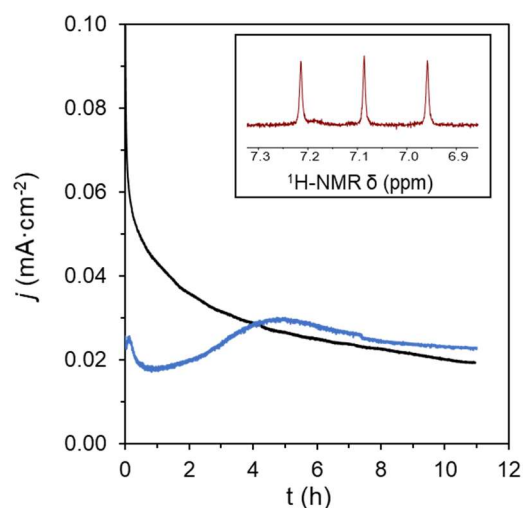


Fig. S15. Current and charge profile for two consecutive CPC at -1.35 V vs $\text{Fc}^{+/0}$ in 0.2 M $[\text{TBA}][\text{BF}_4]$ THF solution containing initially 0.05 mM $\text{Co}(\text{III},\text{N})^+$, 0.05 mM $\text{W}(\text{N}_2)_2$ and 5 mM TsOH, using a GC plate working electrode. After the first CPC (black trace), an extra 100 equiv of TsOH were added through a septum as a concentrated THF solution, and the second CPC was initiated (blue trace). **Inset:** Quantification of generated NH_3 via $^1\text{H-NMR}$ spectroscopy.

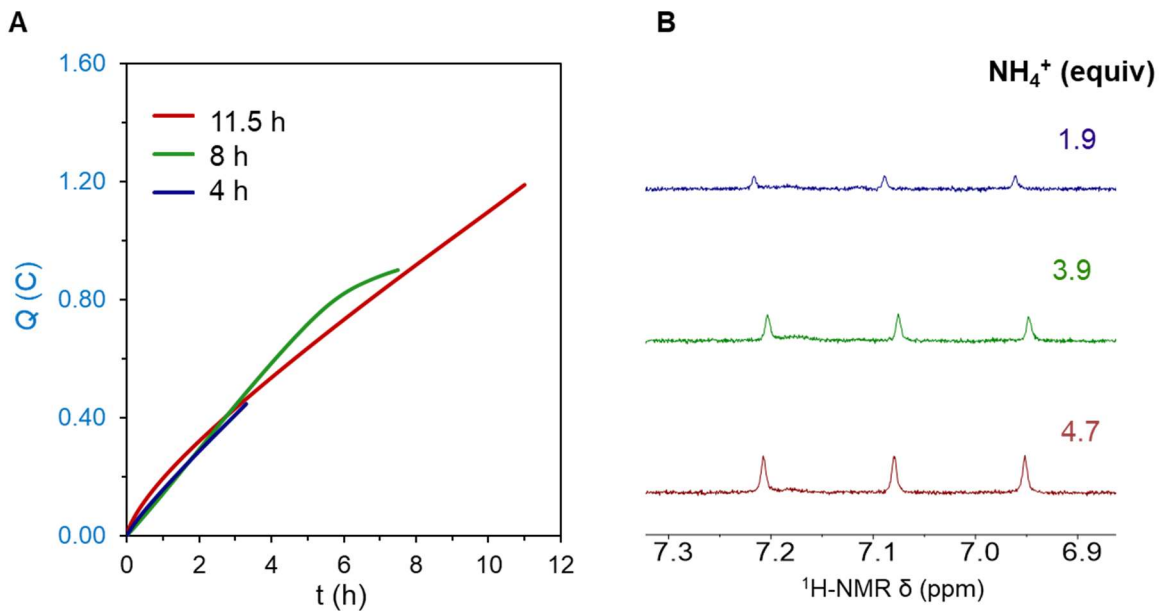


Fig. S16. (A) Charge profile for three different CPC at -1.35 V vs $\text{Fc}^{+/0}$ in 0.2 M $[\text{TBA}][\text{BF}_4]$ THF solution containing 0.05 mM $\text{Co}(\text{III},\text{N})^+$, 0.05 mM $\text{W}(\text{N}_2)_2$ and 5 mM TsOH, using a GC plate working electrode. The three CPC experiments were stopped at different times to confirm that the produced NH_3 is coming from the electrocatalytic process. (B) Quantification of generated NH_3 via $^1\text{H-NMR}$ spectroscopy.

S4. Optimization of N₂RR conditions using W(N₂)₂:

Following initial confirmation of N₂RR by our tandem approach using conditions originally employed in previous reports by Becker and coworkers,² we canvassed different conditions to optimize the production of ammonia. These conditions included the use of different working electrodes, acid concentrations, electrolytes, solvent, and surface areas for the working electrode, as they may influence in electrocatalytic processes in general, and in previous attempts to electrochemical and chemical N₂RR by W and Mo complexes in particular.

Working electrode: GC electrode was initially employed by Becker and coworkers in their electrochemical studies of W(N₂)₂ system.² However, as previously explored by our group, BDD can attenuate the background hydrogen evolution reaction at the surface of the electrode in the presence of TsOH. This is shown in Fig. S17, where CV of both electrodes in the presence of acid are plotted, obtaining comparatively higher background currents with GC. Consistently higher equiv of NH₃ and Faradaic efficiencies were obtained when BDD was used in the CPC experiments compared to GC (entry 1 and 2 in Table S1).

Acid concentration: The acid concentration has a direct influence on background electrocatalytic HER at the electrode, as shown in Fig. S18. As demonstrated by entry 2-5 in Table S1, increasing the acid concentration increases the total production of ammonia, as expected from a higher availability of H⁺, but the Faradaic efficiency drops as a consequence of the relative rate of background HER, increasing more than the rate of N₂RR.

Electrolyte: Initial studies toward electrocatalytic N₂RR using W(N₂)₂ and analogous Mo(N₂)₂ species employed [TBA][BF₄] electrolyte. However, it has been shown that protonation of W(N₂)₂ using HBF₄ generates the corresponding (F)W(NNH₂)₂ hydrazido complex due to abstraction of a F⁻ anion; this species requires a very strong cathodic potential to reduce it and features slow F⁻ dissociation required to proceed in the N₂RR cycle;^{2,19} under our catalytic conditions with [TBA][BF₄] and TsOH, this species is also formed (Fig. S19). Moreover, M(X)(N₂) species (X = Cl⁻, I⁻) can further disproportionate to form the decomposition product M(X)₂ whose reduction to initial M(N₂)₂ requires a strongly reducing potential.²⁰ Therefore, we have explored other electrolytes featuring weak coordinating anions to prevent those issues. Furthermore, we have considered the Li⁺ salts of those anions as they generally feature high conductivity, and the use of Lewis acids has been shown to have favorable effect in the further activation of N₂RR intermediates.²¹ One of the electrolytes fulfilling both aspects, also employed in the initial work by Pickett and coworkers, is [Li][ClO₄], featuring a very high conductivity and with a ClO₄⁻ anion that is very weakly coordinating. However, it is also known that ClO₄⁻ can lead to the oxidation of reduced W and Mo complexes resulting in the formation of off cycle, oxo species. This has been further corroborated under our conditions in the presence of tosic acid by ³¹P-NMR and UV-vis (Fig S20 and S21).²² Therefore, we studied electrolytes based on non-coordinating and chemically inert anions such as OTf⁻, NTf₂⁻ and BAr^F₄⁻. In the case of [Li][OTf], the resulting conductivity of the electrolyte solution is very low, potentially due to formation of ion pairs in solutions that prevent ionic conductivity as previously studied.²³ In contrast, [Na][BAr^F₄] and [Li][NTf₂] lead to highly conductive electrolytes with very similar CV responses of the in situ formed hydrazido species (OTs)W(NNH₂)₂, with redox potentials of around -2.0 V vs Fc⁺⁰, 200 mV lower than in the case of (F)W(NNH₂)₂ (Fig. S22). Our studies showed higher

and more efficient production of ammonia using $[\text{Na}][\text{BAr}^{\text{F}}_4]$ (entry 9 in Table S1), and especially with $[\text{Li}][\text{NTf}_2]$ (entry 11 in Table S1).

Solvent: We have previously found that DME is more resistant to degradation than THF in acidic conditions and have consistently found that ammonia production, in terms of equiv produced and Faradaic efficiency, is increased in DME by comparison (entry 11 and 12 in Table S1).

Catalyst:electrode surface ratio: In order to optimize the electrode/catalyst interphase, minimize the time of CPC, and increase the catalytic current, the use of a high surface area electrode was pursued. We explored the use of GC foam as a high surface area electrode. To minimize the potential consumption of ammonia due to the oxidation process at the counter electrode previously discussed (section S.1.5) the concentration of catalyst was further lowered to 0.01 mM, leading to relatively lower catalytic currents. In this case, a higher number of equiv are obtained (entry 16 in Table S1) per catalyst, highlighting the potential benefit of larger electrode/catalyst interfaces, shorter electrolysis times, and lower catalyst concentrations.

Table S1. Conditions explored for the CPC experiments together with the NH₃ produced and FE.

Entry	Working Electrode	Solvent	Electrolyte	[W] (mM)	[Co] (mM)	[TsOH] (mM)	NH ₃ (equiv/W)	FE (%)
1	GC	THF	[TBA][BF ₄]	0.05	0.05	5.0	4.7	17.8
2	BDD	THF	[TBA][BF ₄]	0.05	0.05	5.0	5.6	20.5
3	BDD	THF	[TBA][BF ₄]	0.05	0.05	2.5	4.6	33.2
4	BDD	THF	[TBA][BF ₄]	0.05	0.05	10.0	6.5	9.4
5	BDD	THF	[TBA][BF ₄]	0.05	0.05	25.0	7.2	5.2
6	BDD	THF	[TBA][BF ₄]	0.05	0.13	5.0	6.7	24.3
7	BDD	THF	[TBA][BF ₄]	0.05	0.25	5.0	7.0	25.5
8	BDD	THF	[Li][ClO ₄]	0.05	0.05	5.0	6.5	23.4
9	BDD	THF	[Na][BAr ^F ₄]	0.05	0.05	5.0	8.7	31.3
10	BDD	THF	[Li][OTf]	0.05	0.05	5.0	7.3	26.4
11	BDD	THF	[Li][NTf ₂]	0.05	0.05	5.0	10.0	36.3
12	BDD	DME	[Li][NTf ₂]	0.05	0.05	5.0	11.5	45.1
13	BDD	DME	[Li][NTf ₂]	0.05	0.05	10.0	15.3	27.7
14	BDD	DME	[Li][NTf ₂]	0.05	0	5.0	0.8	3.0
15	BDD	DME	[Li][NTf ₂]	0	0.05	5.0	-	-
16	GC foam	DME	[Li][NTf ₂]	0.01	0.01	5.0	39.5	42.9

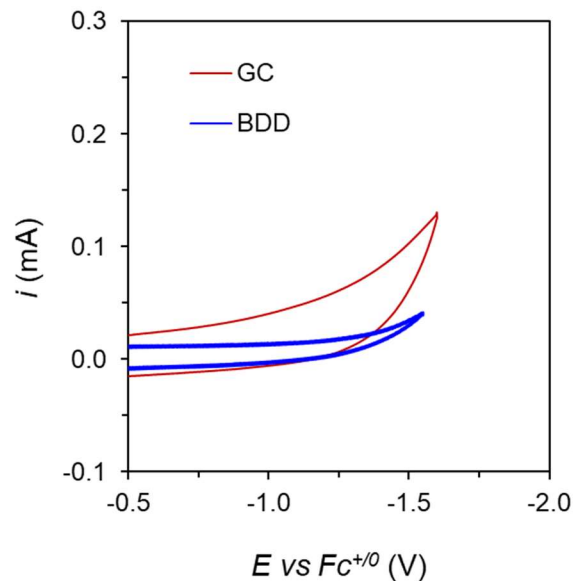


Fig. S17. CV at $100 \text{ mV}\cdot\text{s}^{-1}$ in $0.2 \text{ M [TBA][BF}_4\text{]}$ THF solution containing and 50 mM TsOH , using either a GC (red) or a BDD (blue) plate working electrode.

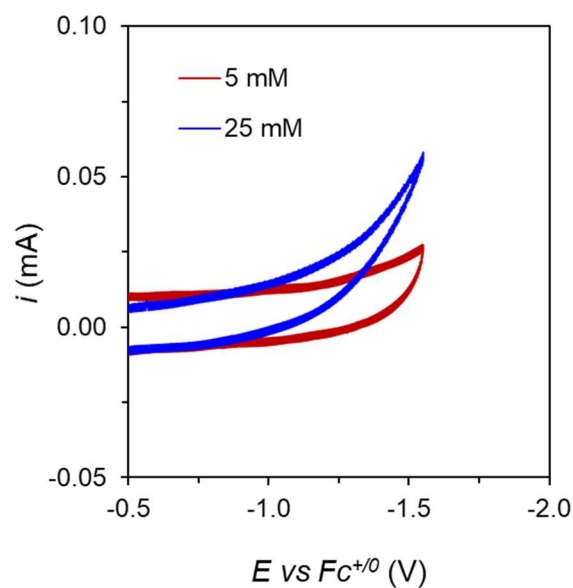


Fig. S18. CV at $100 \text{ mV}\cdot\text{s}^{-1}$ in $0.2 \text{ M [TBA][BF}_4\text{]}$ THF solution containing different concentrations of TsOH and using a BDD plate working electrode. The increase of current with TsOH concentration reflects an increase in the background HER, which in turn has an influence in the Faradaic efficiency obtained from CPC experiments.

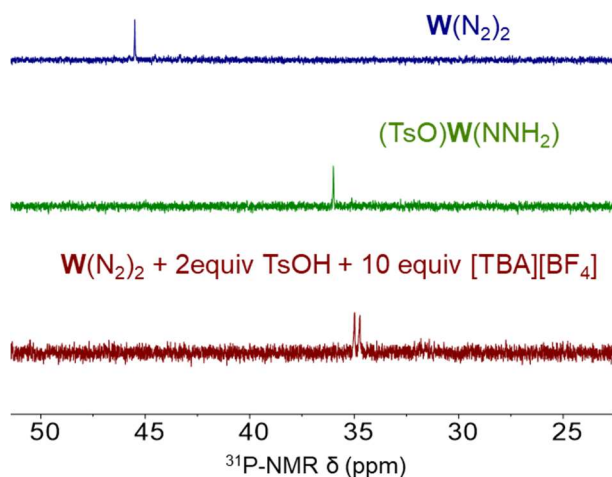


Fig. S19. ³¹P-NMR spectra of a THF solution containing $\mathbf{W}(\text{N}_2)_2$ (blue trace), $(\text{OTs})\mathbf{W}(\text{NNH}_2)^+$ (green trace), and $\mathbf{W}(\text{N}_2)_2$ with 2 equiv of TsOH and 10 equiv $[\text{TBA}][\text{BF}_4]$ as the electrolyte (red trace). The latter shows that protonation of the $\mathbf{W}(\text{N}_2)_2$ in the presence of BF_4^- leads to a hydrazido species distinct from $(\text{OTs})\mathbf{W}(\text{NNH}_2)^+$. The doublet resonance observed is diagnostic for a fluoride complex and this result is hence most consistent with the formation of the known complex $(\text{F})\mathbf{W}(\text{NNH}_2)^+$ instead of $(\text{OTs})\mathbf{W}(\text{NNH}_2)^+$.²⁴

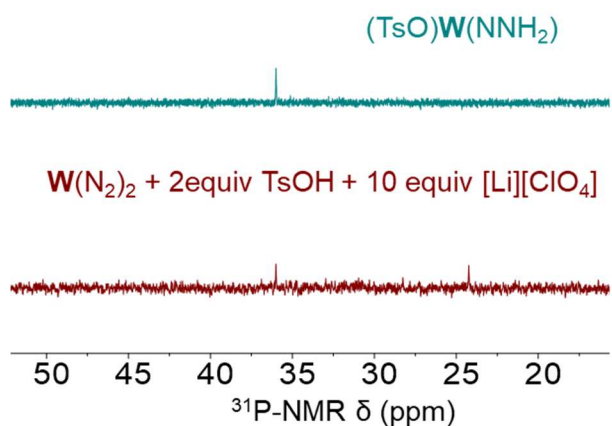


Fig. S20. ³¹P-NMR spectra of a THF solution containing $(\text{OTs})\mathbf{W}(\text{NNH}_2)^+$ (blue trace) and $\mathbf{W}(\text{N}_2)_2$ with 2 equiv of TsOH and 10 equiv $[\text{Li}][\text{ClO}_4]$ (red trace). The latter shows the partial formation of $(\text{OTs})\mathbf{W}(\text{NNH}_2)^+$, together with a second species that we tentatively assign to a previously reported W-trans-dioxo species, based on a previous report.²² This experiment underscores that perchlorate can be non-innocent during electrocatalysis with $[\text{Li}][\text{ClO}_4]$ as the electrolyte.

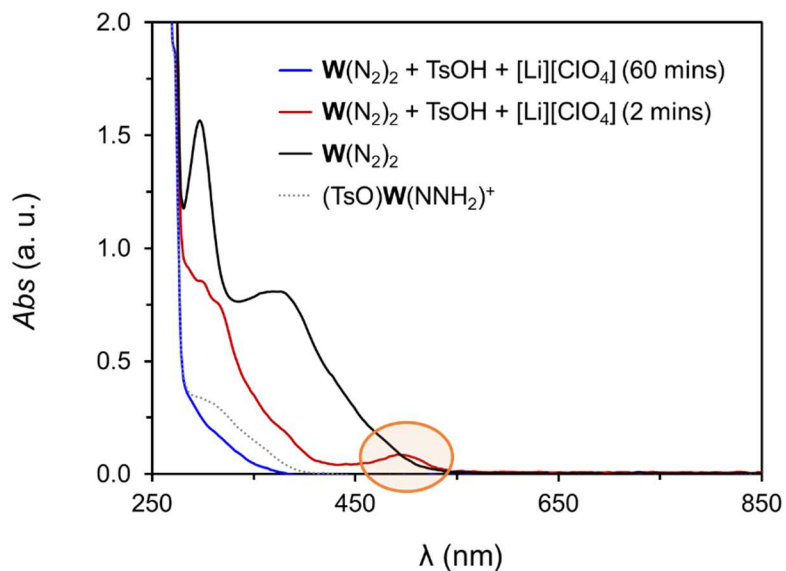


Fig. S21. UV-vis spectra of a THF solution containing 0.05 mM $(\text{OTs})\text{W}(\text{NNH}_2)^+$ (dashed gray trace), 0.05 mM $\text{W}(\text{N}_2)_2$ (black trace), and 0.05 mM $\text{W}(\text{N}_2)_2$ with 2 equiv of TsOH, and 10 equiv $[\text{Li}][\text{ClO}_4]$ after 2 mins (red trace) and 60 mins (blue trace) of reaction. The absorption band at around 500 nm in the red trace supports the formation of the W-oxo species, consistent with literature reports,²² which is unstable and disappears after 60 min of reaction time, leading to lower concentrations of the hydrazido species as compared with a UV-vis sample containing a similar initial concentration of pure $(\text{OTs})\text{W}(\text{NNH}_2)^+$ in THF (grey trace). This experiment underscores that perchlorate can be non-innocent during electrocatalysis with $[\text{Li}][\text{ClO}_4]$ as the electrolyte.

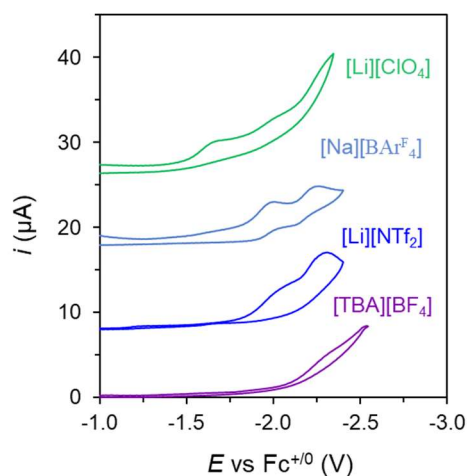


Fig. S22. CV at $100 \text{ mV} \cdot \text{s}^{-1}$ of a THF solution containing 0.05 mM $\text{W}(\text{N}_2)_2$ and 2 equiv of TsOH for the in situ formation of $(\text{TsO})\text{W}(\text{NNH}_2)^+$ using different electrolytes. A BDD disk was used as the working electrode.

S5. Control experiments for electrocatalytic N₂RR:

In order to verify that the produced ammonia derives solely from the electrocatalytic reduction of N₂ by the tandem co-catalytic system, several CPC control experiments were performed to evaluate any possible source of NH₃ contamination, or any other N-containing species as the substrate, for the generation of NH₃. In addition, the content of other N-containing impurities like N₂O, NO_x, NO₂⁻ and NO₃⁻, were probed quantitatively using appropriate analytical methods. These results, summarized below, unequivocally verify atmospheric N₂ as the substrate.

S5.1. Control experiment under Argon atmosphere:

The electrochemical cell was set up as in a typical experiment in a N₂-filled glove box containing the two co-catalysts, the electrolyte solution, the acid, and the three electrodes. Subsequently, the gas-tight cell was brought outside the box and both compartments were bubbled with Argon gas through the septa for 30 mins in order to displace all the N₂. After that time, a CPC was run at -1.35 V vs Fc⁺⁰ as usual (Fig. 23). When the CPC was finished, excess of tosic acid (100 equiv dissolved in 1 mL of DME) was added through the septa with a syringe in order to quench all possible free ammonia in solution as NH₄⁺. Subsequently, the cell was placed in a dry ice/acetone bath at -78 °C to condense possible evaporated ammonia in the headspace. After 10 min at this temperature, the electrochemical cell was brought to room temperature and allowed to stir for another 10 min in the presence of the excess acid. Finally, the cell was opened, and the electrolyte solution was treated as previously described (section S.2.1) for quantification of ammonia. The total ammonia produced during this experiment was below 0.1 equiv (< 10 nmol). This experiment provides evidence against contamination of NH₃ in the electrochemical set up, as well as the absence of any other N-containing species that can act as an N-source for the generation of ammonia upon reduction, such as the [Li][NTf₂], or NO₂⁻ or NO₃⁻ in the electrolyte solution.

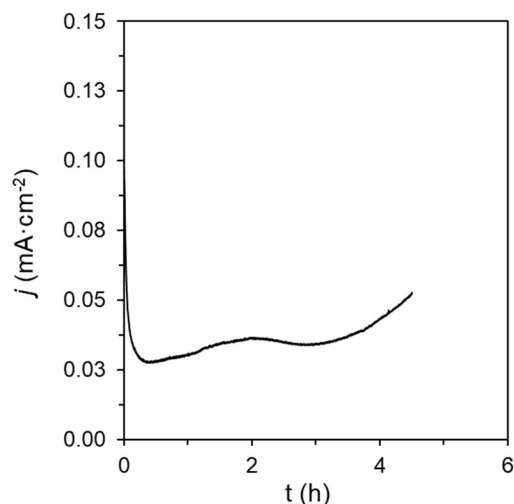


Fig. S23. Current profile for a CPC at -1.35 V vs Fc⁺⁰ in 0.1 M [Li][NTf₂] DME solution containing 0.05 mM Co(III,N)⁺, 0.05 mM W(N₂)₂ and 5 mM TsOH, under Argon atmosphere using a BDD plate working electrode.

S5.2 Control experiment using $^{15}\text{N}_2$ atmosphere:

The electrochemical cell was set up as in a typical experiment in a N_2 -filled glove box containing the two co-catalysts, the electrolyte solution, the acid, and the three electrodes. The gas-tight cell was brought outside the box and both compartments were bubbled with Argon gas through the septa for 30 mins in order to make sure all the $^{14}\text{N}_2$ was displaced, as evidenced in previous control experiment under Argon atmosphere. Subsequently, the cell was then bubbled with $^{15}\text{N}_2$ for 5 mins to substitute the Ar, and then left to equilibrate for 5 more mins under the $^{15}\text{N}_2$ atmosphere. After that time, a CPC was run at -1.35 V vs $\text{Fc}^{+/0}$ using the typical procedure (Fig. S24). When the CPC was finished, an excess of tosic acid (twice as much as theoretical $^{15}\text{NH}_3$ produced) was added through the septa with a syringe in order to quench all possible free $^{15}\text{NH}_3$ in solution as $^{15}\text{NH}_4^+$. Subsequently, the cell was placed in a dry ice/acetone bath at $-78\text{ }^\circ\text{C}$ in order to condense possible evaporated ammonia in the headspace. After 10 min at this temperature, the electrochemical cell was brought to room temperature and allowed to stir for another 10 min in the presence of the excess acid. Finally, the cell was opened, and the electrolyte solution was treated as previously described (section S.2.1) for quantification of ammonia. This experiment provides evidence against contamination of $^{14}\text{NH}_3$ in the electrochemical set up, as well as the absence of any other N-containing species that could act as N-source for the generation of ammonia upon reduction such as N_2O , NO_x gasses in the gas supply, or $[\text{Li}][\text{NTf}_2]$, NO_2^- , or NO_3^- in the electrolyte solution.

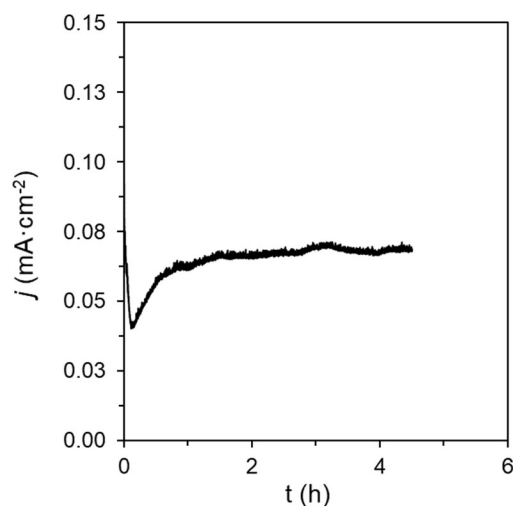


Fig. S24. Current profile for a CPC at -1.35 V vs $\text{Fc}^{+/0}$ in 0.1 M $[\text{Li}][\text{NTf}_2]$ DME solution containing 0.05 mM $\text{Co}(\text{III},\text{N})^+$, 0.05 mM $\text{W}(\text{N}_2)_2$ and 5 mM TsOH, under $^{15}\text{N}_2$ atmosphere using a BDD plate working electrode.

S5.3 Control experiment in the absence of catalysts:

In order to further support that the source of produced ammonia is the electrochemical reduction of N_2 by the tandem co-catalytic system, instead of any NH_3 contamination or direct reduction of N_2O , NO_x , $[\text{Li}][\text{NTf}_2]$, NO_2^- or NO_3^- at the electrode, a CPC was also performed in the absence of $\text{Co}(\text{III},\text{N})^+$ and $\text{W}(\text{N}_2)_2$ (Fig. S25).

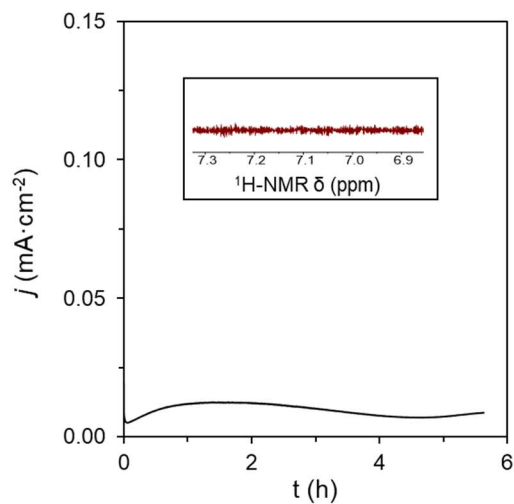


Fig. S25. Current profile for a CPC at -1.35 V vs $\text{Fc}^{+/0}$ in 0.1 M $[\text{Li}][\text{NTf}_2]$ DME solution containing 5 mM TsOH, under $^{14}\text{N}_2$ atmosphere using a BDD plate working electrode. **Inset:** Quantification of NH_3 via $^1\text{H-NMR}$ under previous conditions.

S5.4 Quantification of N₂O impurities in the N₂ gas supply via GC-TCD:

The content of N₂O in the N₂ gas supplies for both ¹⁴N₂ and ¹⁵N₂ was determined by gas chromatography coupled to a thermal conductivity detector (GC-TCD). The method employed included a detector temperature of 250 °C, inlet temperature of 150 °C, and an oven maximum temperature of 275 °C. Calibration of the N₂O signal was performed by injecting pure N₂O gas and a standard mixture of N₂ containing 1 ppm of N₂O using a gas-tight Hamilton syringe. Under these conditions, an N₂O signal appears at a retention time of 6.8 mins.

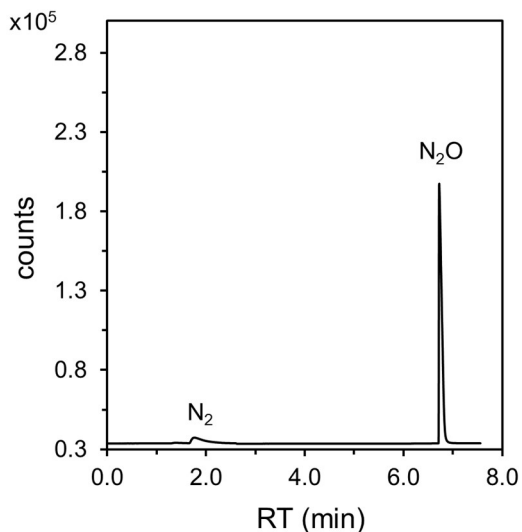


Fig. S26. Gas chromatogram of an injection of N₂O gas for determination of the retention time. The peak at around 1.8 mins correspond to trace N₂ gas.

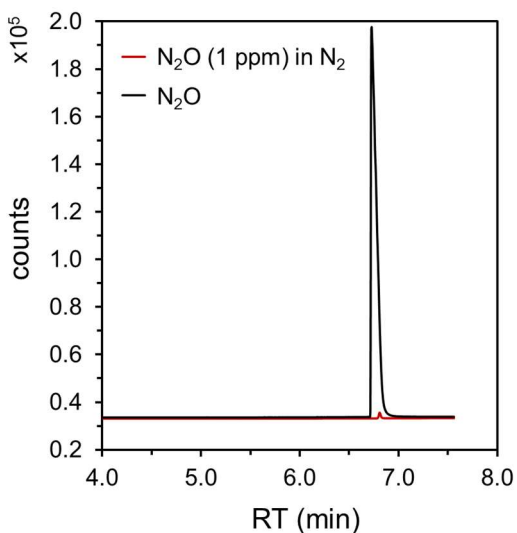


Fig. S27. Gas chromatogram of an injection of N₂O gas (black trace) and a mixture of N₂ with 1 ppm of N₂O for calibration of the area.

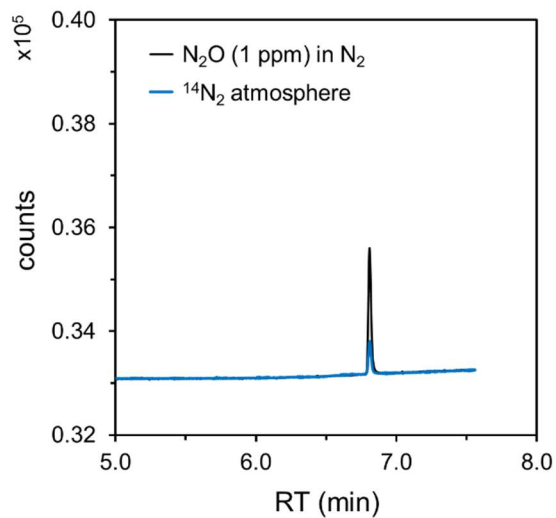


Fig. S28. Gas chromatogram of an injection of a mixture of N₂ with 1 ppm of N₂O (black trace) and the ¹⁴N₂ gas from the glove box employed for the N₂RR experiments (blue trace).

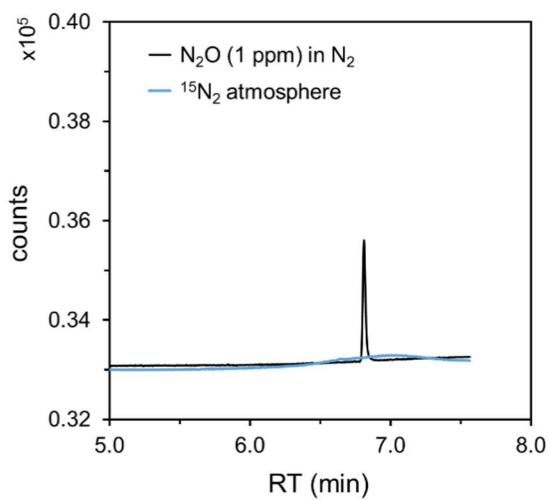


Fig. S29. Gas chromatogram of an injection of a mixture of N₂ with 1 ppm of N₂O (black trace) and the ¹⁵N₂ gas from the gas cylinder employed for the control N₂RR experiment (blue trace).

S5.5 Quantification of NO_x impurities in the N_2 gas supply via the Griess method:

Determination of the NO_x impurities in the gas supplies was performed by their conversion to NO_2^- and NO_3^- in basic media and quantification of the latter by the Griess method.¹³ Specifically, the electrochemical cell exposed to either $^{14}\text{N}_2$ or $^{15}\text{N}_2$ atmosphere employed in the N_2RR experiments was filled with 6 mL of 0.1 M KOH aqueous solution left stirring over 2 h. Any NO_x impurity is assumed to be quantitatively converted into NO_2^- or NO_3^- in this basic solution, and these compounds can in turn be quantified using the Griess spectrophotometric method with the color development solutions previously explained in section S1.2. This was done by sampling 500 μL of the KOH trap solution and adding 500 μL of a 0.1 M HCl aqueous solution, 25 μL of the sulphanilamide solution and 25 μL of the N-1-naphthylethylenediamine dihydrochloride solution. The resulting mixture was incubated for 20 min at room temperature and subsequently the UV-vis spectrum was obtained in a 1 cm quartz cuvette. Absorption at 550 nm enables evaluation of the NO_2^- content upon calibration. For the calibration plots, standard solutions containing different concentrations of NaNO_2 in 0.1 M KOH were subjected to the same color development procedure. For quantification of NO_3^- , the solution used in the quantification of NO_2^- was reacted with 50 μL of a vanadium(III) chloride (VCl_3) solution in 6 M aqueous HCl and incubated at 60 °C during 25 mins in order to quantitatively reduce the NO_3^- to NO_2^- . After that time, the solution was brought to room temperature and the absorption spectrum was again obtained for evaluation of the band at 550 nm. No significant content of NO_x impurities was found in either $^{14}\text{N}_2$ or $^{15}\text{N}_2$ gas supplies corresponding to the amounts of NH_3 produced in this work, supporting N_2 as the sole source of NH_3 .

Calibration plots were performed for both NO_2^- and NO_3^- using their corresponding sodium salts as standard samples and preparing solutions in a range of relevant concentrations. Both calibration plots were linear with $R^2 > 0.99$, and the regression lines were employed for direct, quantitative determination of the NO_2^- and NO_3^- content in the different samples to analyze.

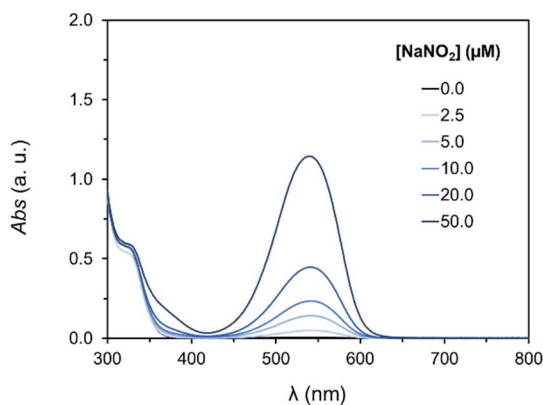


Fig. S30. UV-vis spectra of solutions containing different concentrations of NaNO_2 for calibration purposes subjected to the previously described protocol for quantification based on the Griess method.

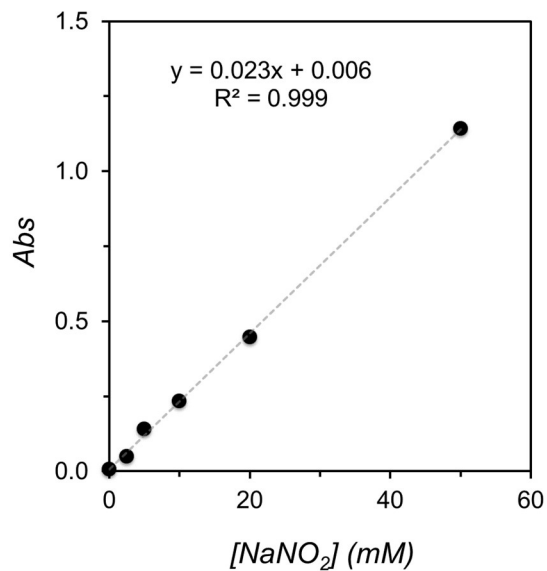


Fig. S31. Calibration plot of the Griess analysis for NO_2^- with the corresponding linear regression.

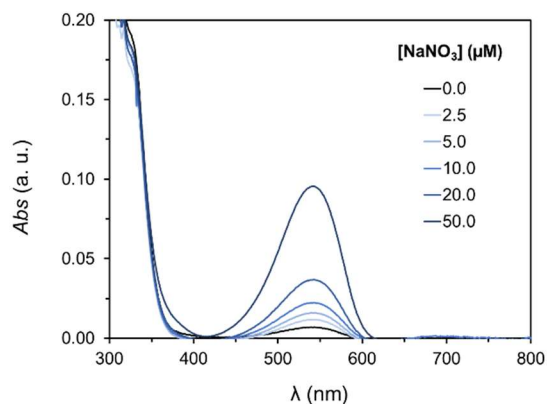


Fig. S32. UV-vis spectra of solutions containing different concentrations of NaNO_3 for calibration purposes subjected to the previously described protocol for quantification based on the Griess method.

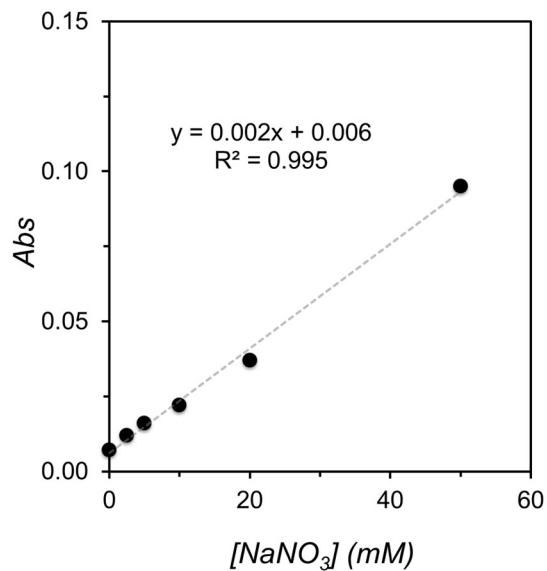


Fig. S33. Calibration plot of the Griess analysis for NO_3^- with the corresponding linear regression.

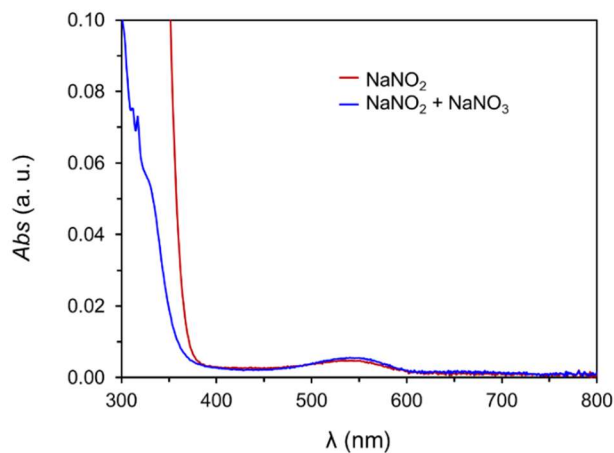


Fig. S34. UV-vis spectra for the Griess analysis of a 0.1 M KOH solution exposed to the $^{14}\text{N}_2$ gas employed in the N_2RR CPC experiments for the determination of the NO_2^- and NO_3^- deriving from NO_x impurities. The content of $\text{NO}_2^- + \text{NO}_3^-$ is below 0.2 nmol based on the calibration plots.

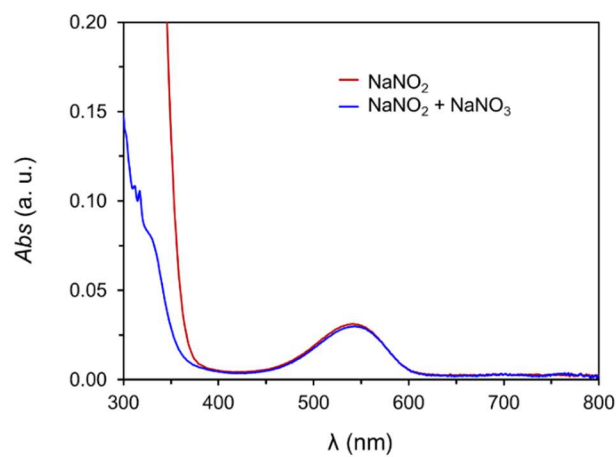


Fig. S35. UV-vis spectra for the Griess analysis of a 0.1 M KOH solution exposed to the ¹⁵N₂ gas employed in the control N₂RR CPC experiments for the determination of the NO₂⁻ and NO₃⁻ deriving from NO_x impurities. The content of NO₂⁻ + NO₃⁻ is below 2.1 nmol based on the calibration plots.

S5.6 Quantification of NO_2^- and NO_3^- impurities in the electrolyte via Griess method:

The content of NO_2^- and NO_3^- impurities in the electrolyte solution was also determined using the Griess method and the calibration plots previously obtained. For that, THF and DME solutions containing either 0.2 M [TBA][BF₄] or 0.1 M [Li][NTf₂] and 5 mM TsOH were prepared under ¹⁴N₂ atmosphere in a glove box following similar procedure as in the CPC experiments. The solution was stirred for 2 h and the Griess method was performed as detailed above. The amount of NO_2^- or NO_3^- impurities were trace from the electrolyte solutions and insignificant relevant to the amounts of NH₃ produced in this work, supporting along with other controls that N₂ as the sole source of NH₃ produced.

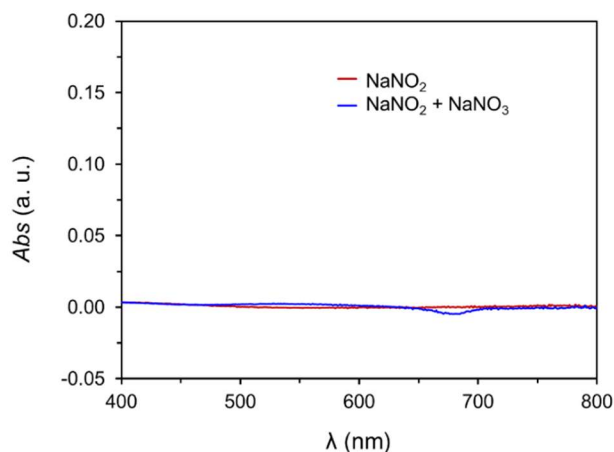


Fig. S36. UV-vis spectra for the Griess analysis of a THF solution containing 0.2 M [TBA][BF₄] and 5 mM TsOH, as employed in the CPC experiments, for the determination of the NO_2^- (red trace) and NO_3^- (blue trace). The content of $\text{NO}_2^- + \text{NO}_3^-$ is below 0.1 nmol based on the calibration plots.

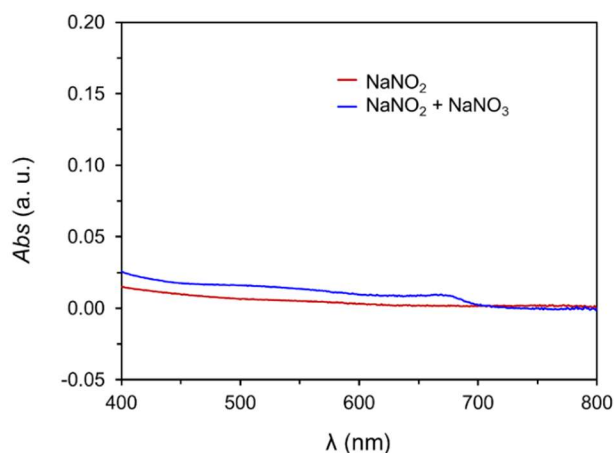


Fig. S37. UV-vis spectra for the Griess analysis of a THF solution containing 0.1 M [Li][NTf₂] and 5 mM TsOH, as employed in the CPC experiments, for the determination of the NO_2^- (red

trace) and NO_3^- (blue trace). The content of $\text{NO}_2^- + \text{NO}_3^-$ is below 0.1 nmol based on the calibration plots.

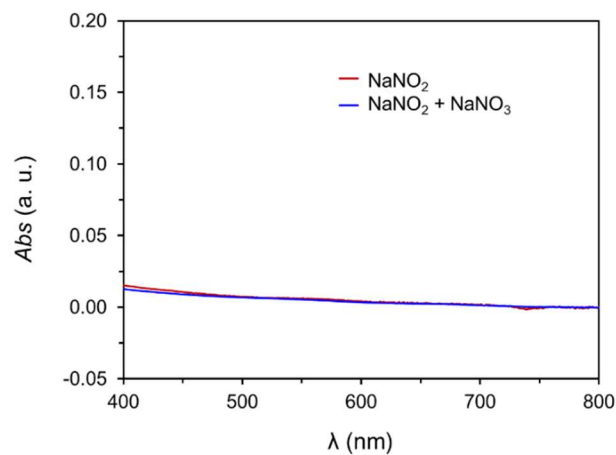


Fig. S38. UV-vis spectra for the Griess analysis of a DME solution containing 0.1 M $[\text{Li}][\text{NTf}_2]$ and 5 mM TsOH, as employed in the CPC experiments, for the determination of the NO_2^- (red trace) and NO_3^- (blue trace). The content of $\text{NO}_2^- + \text{NO}_3^-$ is below 0.1 nmol based on the calibration plots.

S6. Protonation of $\mathbf{W(N_2)_2}$:

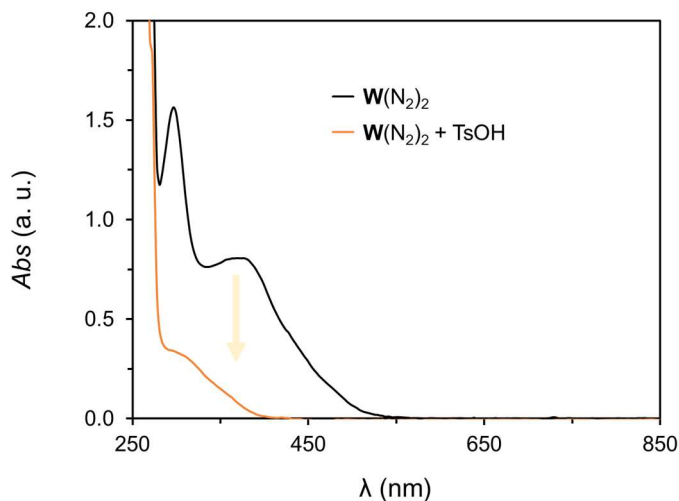


Fig. S39. UV-vis spectra of a THF solution containing 0.05 mM $\mathbf{W(N_2)_2}$ before (black trace) and after (yellow trace) addition of 100 equiv of TsOH for the quantitative formation of the hydrazido intermediate $(\text{TsO})\mathbf{W}(\text{NNH}_2)^+$.

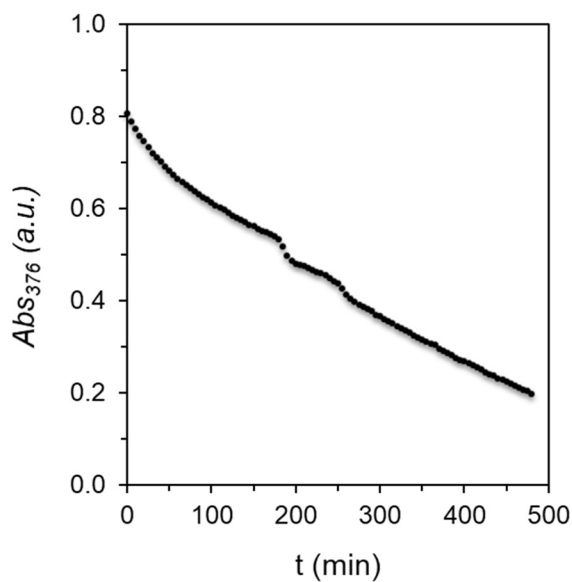


Fig. S40. Time evolution of the absorption at 376 nm of a THF solution containing 0.05 mM $\mathbf{W(N_2)_2}$ after addition of 100 equiv of TsOH for the quantitative formation of the hydrazido intermediate $(\text{TsO})\mathbf{W}(\text{NNH}_2)^+$.

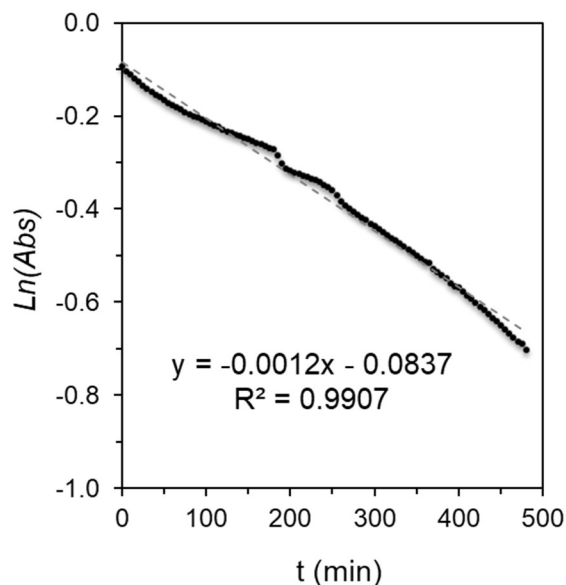


Fig. S41. Plot of the natural logarithm of the absorption at 376 nm versus time of a THF solution containing 0.05 mM $\mathbf{W}(\text{N}_2)_2$ after addition of 100 equiv of TsOH for the quantitative formation of the hydrazido intermediate $(\text{TsO})\mathbf{W}(\text{NNH}_2)^+$. The plot reflects a pseudo first order reaction with a k_{obs} of 0.0012 min^{-1} for the protonation of the dinitrogen complex, consistent with previous work studying these protonation steps.²⁵

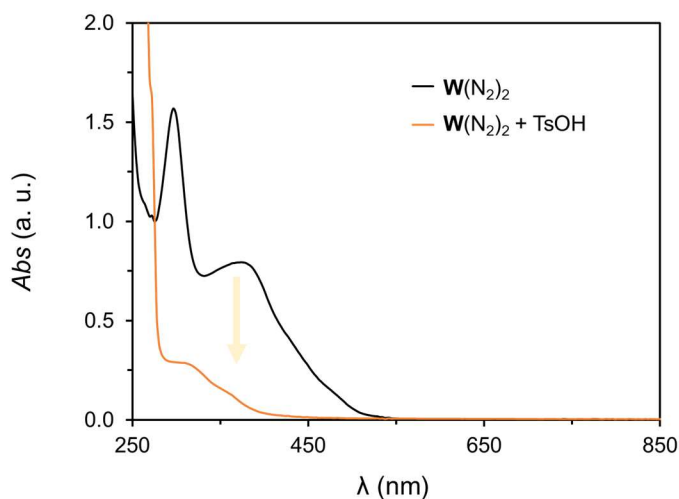


Fig. S42. UV-vis spectra of a THF solution containing 0.1 M $[\text{Li}][\text{NTf}_2]$ and 0.05 mM $\mathbf{W}(\text{N}_2)_2$ before (black trace) and after (yellow trace) addition of 100 equiv of TsOH for the quantitative formation of the hydrazido intermediate $(\text{TsO})\mathbf{W}(\text{NNH}_2)^+$.

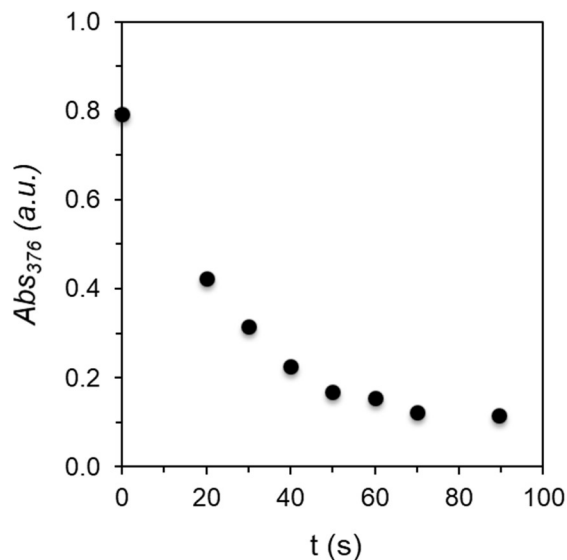


Fig. S43. Time evolution of the absorption at 376 nm of a THF solution containing 0.1 M [Li][NTf₂] and 0.05 mM **W**(N₂)₂ after addition of 100 equiv of TsOH for the quantitative formation of the hydrazido intermediate (TsO)**W**(NNH₂)⁺.

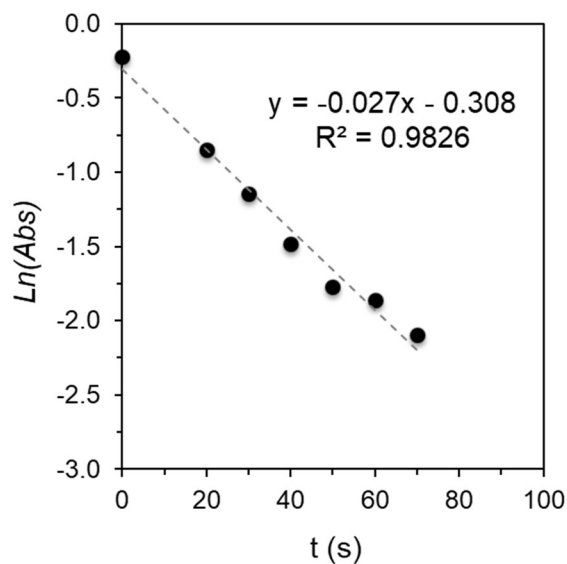


Fig. S44. Plot of the natural logarithm of the absorption at 376 nm versus time of a THF solution containing 0.1 M [Li][NTf₂], 0.05 mM **W**(N₂)₂ after addition of 100 equiv of TsOH for the quantitative formation of the hydrazido intermediate (TsO)**W**(NNH₂)⁺. The plot reflects a pseudo first order reaction with a k_{obs} of 0.027 s⁻¹ for the protonation of the dinitrogen complex, consistent with its influence in the overall rate of catalysis and the observed partial order in acid. The faster rate than observed with [TBA][BF₄] is consistent with a potential role of the [Li][NTf₂] in activating the dinitrogen complex and/or stabilizing the hydrogen bonded intermediates.²⁶

S7. Chemical CPET reactions:

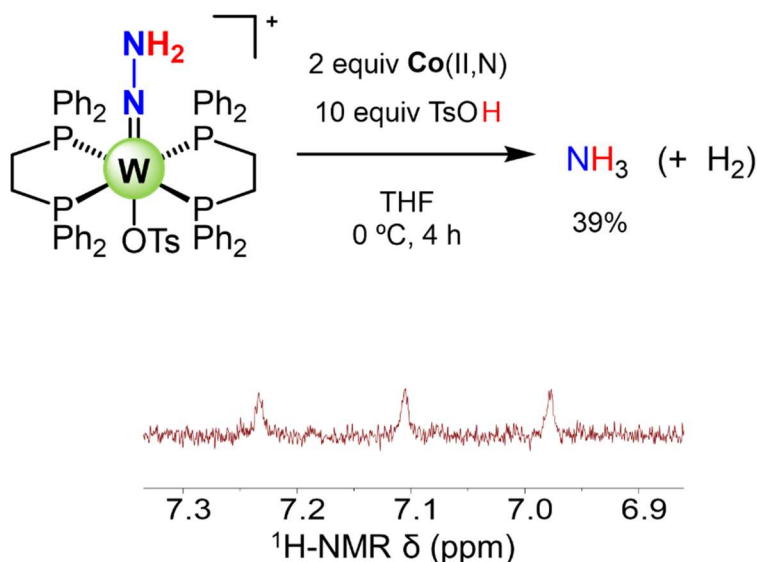


Fig. S45. Chemical reaction of 0.5 mM $(\text{TsO})\text{W}(\text{NNH}_2)^+$ in THF with 2 equiv $\text{Co}(\text{II},\text{N})$ in the presence of excess acid and the corresponding $^1\text{H-NMR}$ spectrum after work up for the quantification of NH_3 produced. These results show the capability of $\text{Co}(\text{II},\text{NH})^+$, formed after rapid protonation of $\text{Co}(\text{II},\text{N})$, to reduce the $(\text{TsO})\text{W}(\text{NNH}_2)^+$ intermediate, leading to the formation of ammonia.

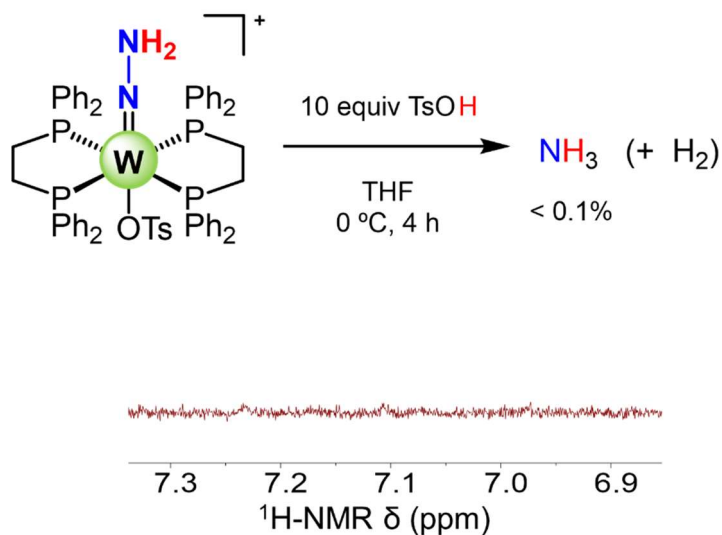


Fig. S46. Chemical reaction of 0.5 mM $(\text{TsO})\text{W}(\text{NNH}_2)^+$ in THF with excess acid in the absence of the $\text{Co}(\text{II},\text{N})$ mediator and the corresponding $^1\text{H-NMR}$ spectrum after work up for the quantification of NH_3 produced (< 3%). These results show the absence of significant reactivity between the $(\text{TsO})\text{W}(\text{NNH}_2)^+$ intermediate and acid leading to the formation of ammonia. The trace NH_3 observed may arise from a disproportionation reaction, for example where a tungsten complex serves as a source of electrons.²⁷

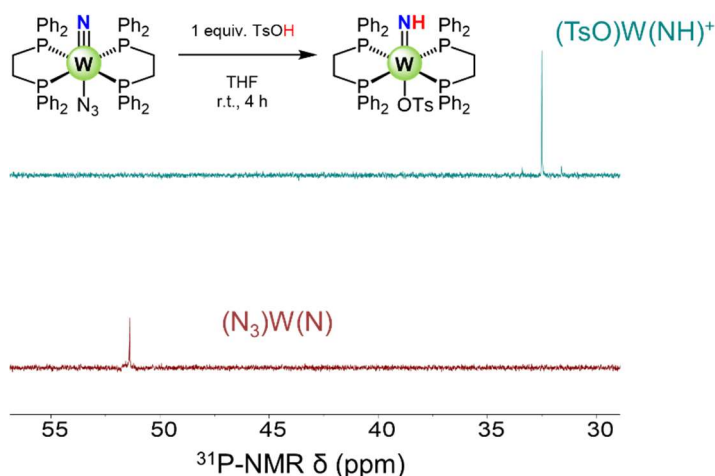


Fig. S47. $^{31}\text{P-NMR}$ spectrum of 0.5 mM $(\text{N}_3)\text{W}(\text{N})$ in THF before (red trace) and after (blue trace) addition of 1 equiv TsOH, showing the formation of the imido intermediate $(\text{X})\text{W}(\text{NH})^+$ ($\text{X} = \text{OTs}$ or N_3).

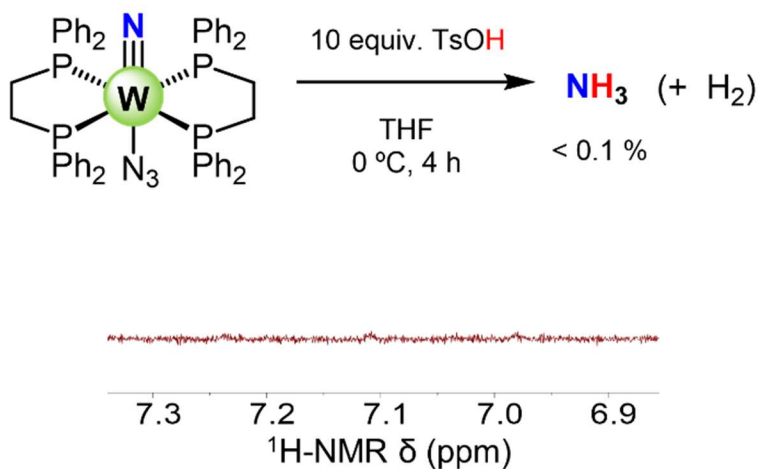


Fig. S48. Chemical reaction of 0.5 mM $(\text{N}_3)\text{W}(\text{N})$ in THF with excess acid in the absence of the $\text{Co}(\text{II},\text{N})$ mediator and the corresponding $^1\text{H-NMR}$ spectrum after work up for the quantification of NH_3 produced ($< 3\%$). These results show the absence of significant reactivity between the $(\text{TsO})\text{W}(\text{NH})^+$ intermediate, formed by in situ protonation of $(\text{N}_3)\text{W}(\text{N})$, and acid leading to the formation of ammonia. The trace NH_3 observed may arise from a disproportionation reaction, for example where a tungsten complex serves as a source of electrons.²⁷

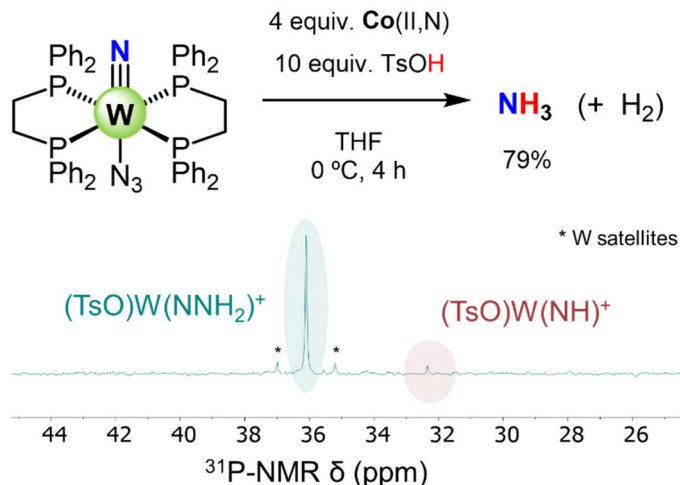


Fig. S49. Chemical reaction of 0.5 mM $(N_3)W(N)$ in THF with 4 equiv $Co(II,N)$ in the presence of excess acid and the corresponding ^{31}P -NMR spectrum. The $TsOH$ was added prior to the addition of $Co(II,N)$ for the formation of $(TsO)W(NH)^+$. These results evidence the capability of $Co(II,NH)^+$, formed after rapid protonation of $Co(II,N)$, to reduce the $(TsO)W(NH)^+$ intermediate, formed by in situ protonation of $(N_3)W(N)$, towards formation of ammonia, and regeneration of $W(N_2)_2$, which then undergoes protonation with the excess of acid to form $(TsO)W(NNH_2)^+$.

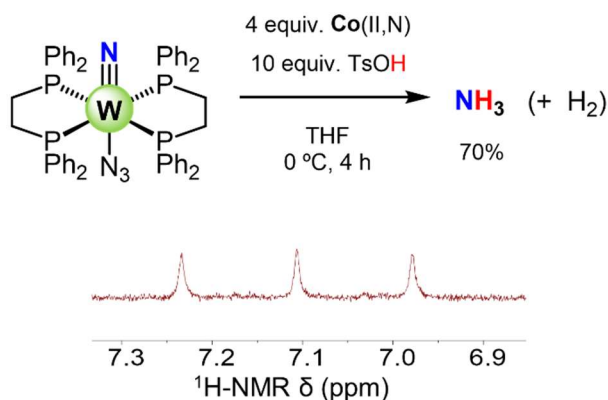


Fig. S50. Chemical reaction of 0.5 mM $(N_3)W(N)$ in THF with 4 equiv $Co(II,N)$ in the presence of excess acid and the corresponding 1H -NMR spectrum after work up for the quantification of NH_3 produced. The $TsOH$ was added previous to the addition of $Co(II,N)$ for the formation of $(TsO)W(NH)^+$. These results show the capability of $Co(II,NH)^+$, formed after rapid protonation of $Co(II,N)$, to reduce the $(TsO)W(NH)^+$ intermediate (formed by previous protonation of $(N_3)W(N)$) towards formation of ammonia.

S8. Mechanistic analysis via cyclic voltammetry:

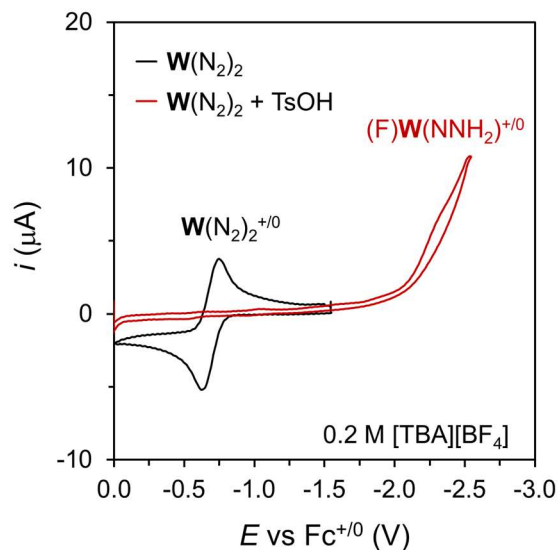


Fig. S51. CV at $100 \text{ mV}\cdot\text{s}^{-1}$ of a $0.2 \text{ M [TBA][BF}_4\text{]}$ THF solution containing $0.5 \text{ mM W(N}_2\text{)}$ before (black trace) and after (red trace) addition of 2 equiv of TsOH showing the formation of $(\text{F})\text{W(NNH}_2\text{)}^+$.

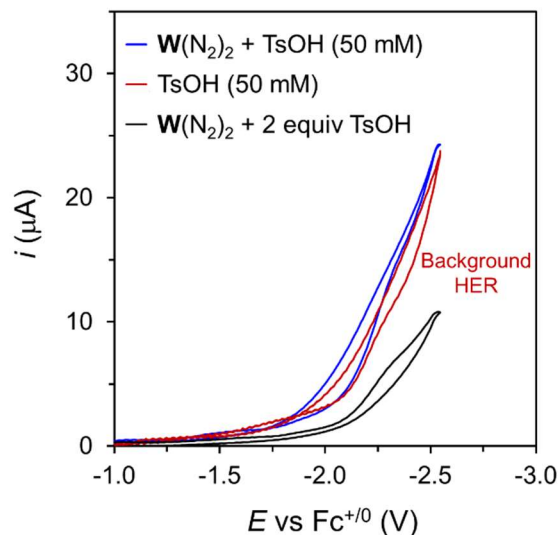


Fig. S52. CV at $100 \text{ mV}\cdot\text{s}^{-1}$ of a $0.2 \text{ M [TBA][BF}_4\text{]}$ THF solution containing $0.5 \text{ mM W(N}_2\text{)}$ and 2 equiv of TsOH (black trace), $0.5 \text{ mM W(N}_2\text{)}$ and 50 mM TsOH (blue trace), and only 50 mM TsOH (red trace). These results show the similar electrochemical response with excess TsOH in the presence and absence of $\text{W(N}_2\text{)}$ consistent with dominant electrocatalytic HER mediated by the electrode under these conditions.

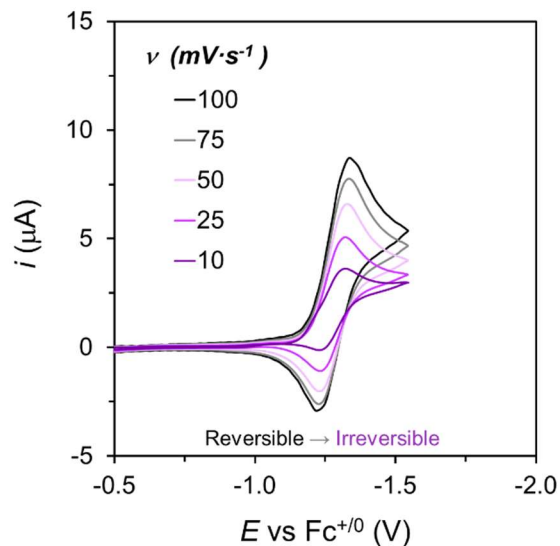


Fig. S53. Variable scan rate CVs of a 0.2 M [TBA][BF₄] THF solution containing 0.5 mM Co(III,N)⁺, 0.5 mM W(N₂) and 50 mM TsOH showing how at the slower scan rates the reversibility decreases, consistent with a catalytic process coupled to the reduction of in situ generated Co(III,NH)²⁺ to Co(II,NH)⁺.

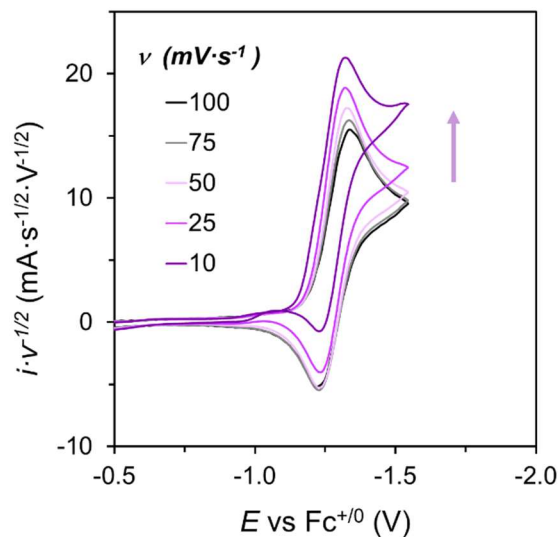


Fig. S54. CVs normalized by the scan rate of a 0.2 M [TBA][BF₄] THF solution containing 0.5 mM Co(III,N)⁺, 0.5 mM W(N₂) and 50 mM TsOH. These results show how at slower scan rates the reversibility decreases and the normalized current increases, consistent with a catalytic process coupled to the reduction of in situ generated Co(III,NH)²⁺ to Co(II,NH)⁺.

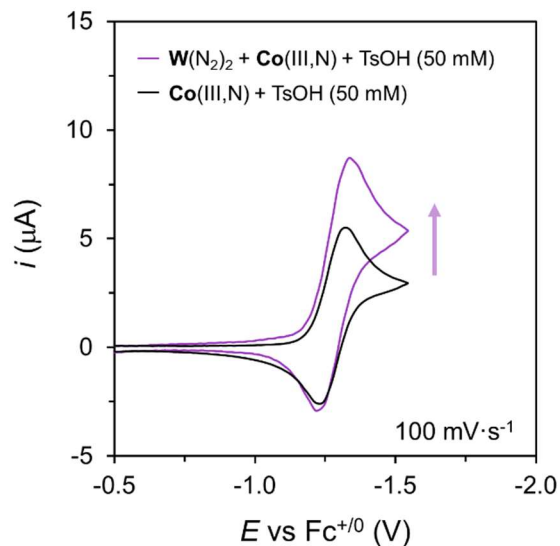


Fig. S55. CVs at $100 \text{ mV}\cdot\text{s}^{-1}$ of a 0.2 M $[\text{TBA}][\text{BF}_4]$ THF solution containing 0.5 mM Co(III,N)^+ and 50 mM TsOH with (purple trace) and without (black trace) 0.5 mM $\text{W(N}_2)$. These results show the increase in the current associated with the reduction of Co(III,NH)^{2+} to Co(II,NH)^+ , consistent with tandem electrocatalysis.

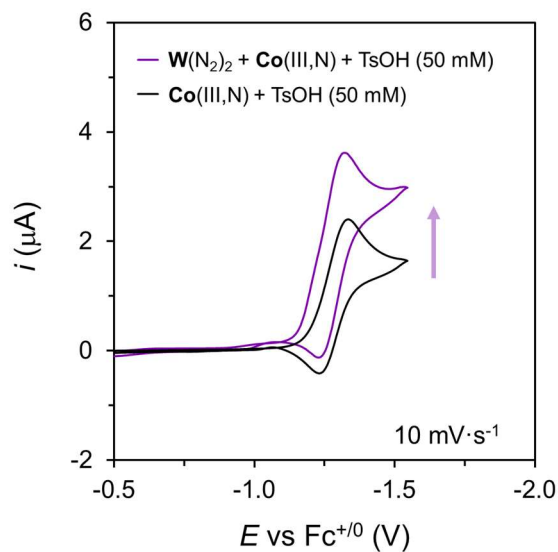


Fig. S56. CVs at $10 \text{ mV}\cdot\text{s}^{-1}$ of a 0.2 M $[\text{TBA}][\text{BF}_4]$ THF solution containing 0.5 mM Co(III,N)^+ and 50 mM TsOH with (purple trace) and without (black trace) 0.5 mM $\text{W(N}_2)$. These results show an increase in the current associated with the reduction of Co(III,NH)^{2+} to Co(II,NH)^+ , consistent with tandem electrocatalysis.

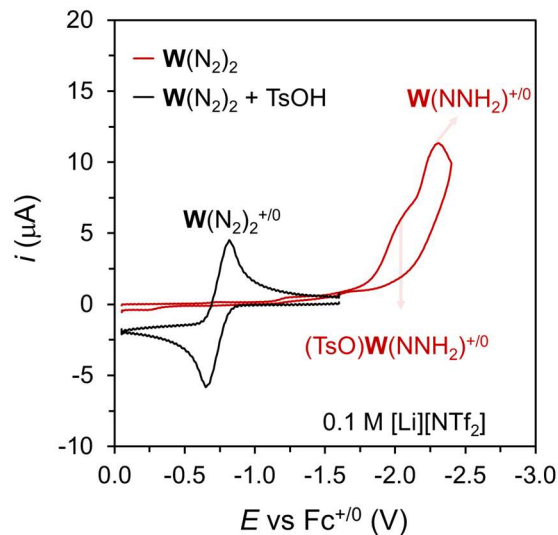


Fig. S57. CV at $100 \text{ mV}\cdot\text{s}^{-1}$ of a $0.1 \text{ M [Li][NTf}_2\text{]}$ THF solution containing $0.5 \text{ mM W(N}_2\text{)}$ before (black trace) and after (red trace) addition of 2 equiv of TsOH, showing the formation of $(\text{OTs})\text{W(NNH}_2\text{)}^+$.

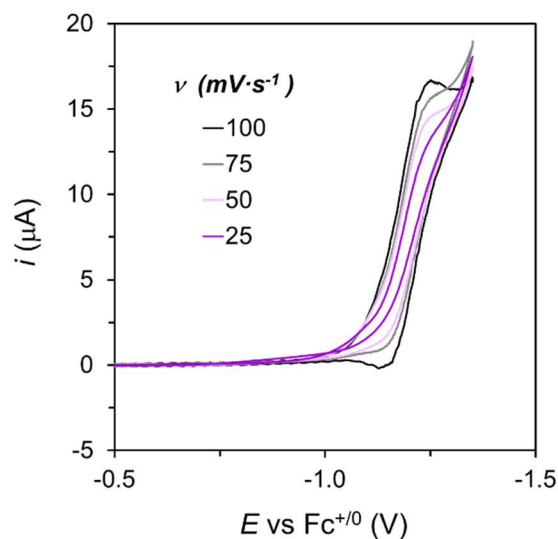


Fig. S58. Variable scan rates CVs of a $0.1 \text{ M [Li][NTf}_2\text{]}$ THF solution containing $0.5 \text{ mM Co(III,N)}^+$, $0.5 \text{ mM W(N}_2\text{)}$ and 50 mM TsOH , showing an irreversible electrocatalytic response as compared to the one electron wave of Co(III,NH)^+ . The irreversibility increases as the scan rate decreases.

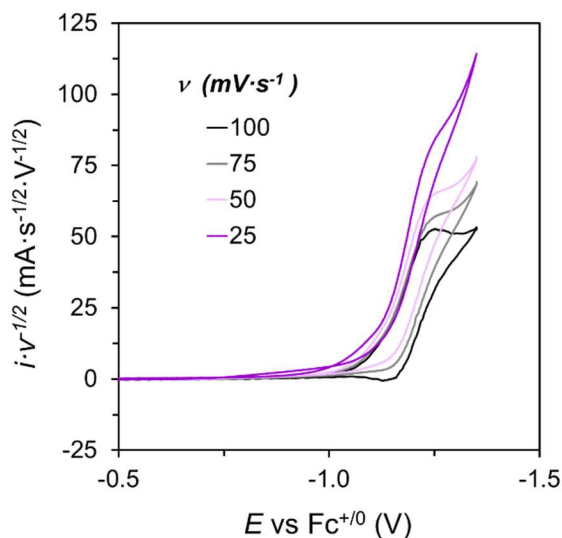


Fig. S59. CVs normalized by the scan rate of a 0.1 M [Li][NTf₂] THF solution containing 0.5 mM Co(III,N)⁺, 0.5 mM W(N₂) and 50 mM TsOH. These results show that at slower scan rates the reversibility decreases and the normalized current increases, consistent with a catalytic process coupled to the reduction of in situ generated Co(III,NH)²⁺ to Co(II,NH)⁺.

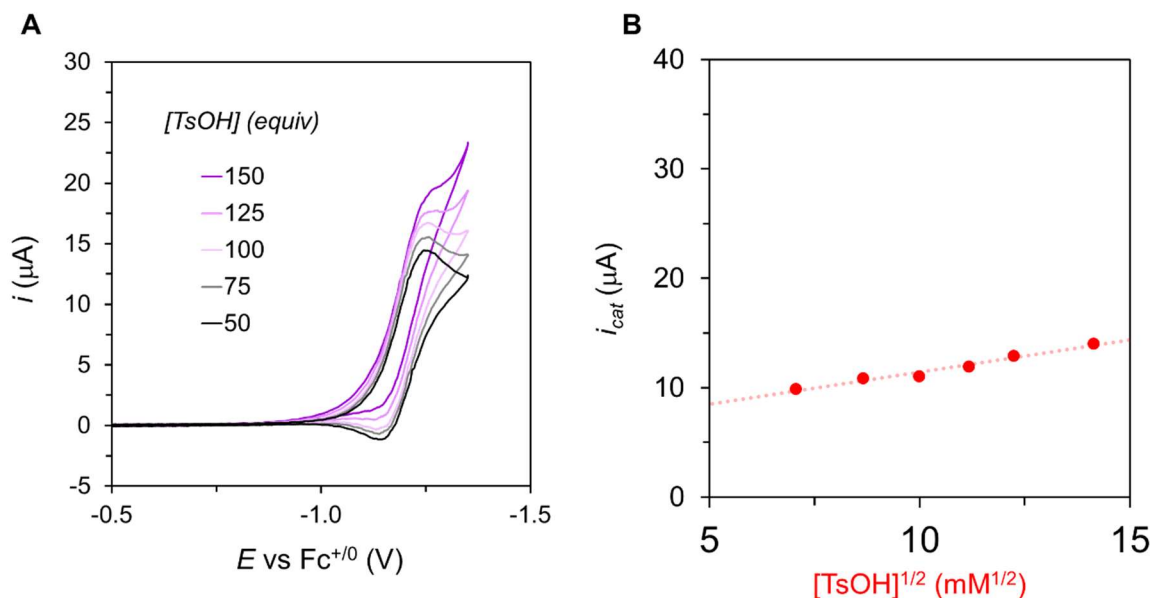


Fig. S60. (A) CVs at 100 mV·s⁻¹ of a 0.1 M [Li][NTf₂] THF solution containing 0.5 mM Co(III,N)⁺, 0.5 mM W(N₂) and increasing concentrations of TsOH, evidencing a partial positive order in acid for the electrocatalytic process. (B) Dependence of the catalytic current extracted from background corrected CVs with the concentration of TsOH, reflecting the partial positive order in acid of the electrocatalytic process.

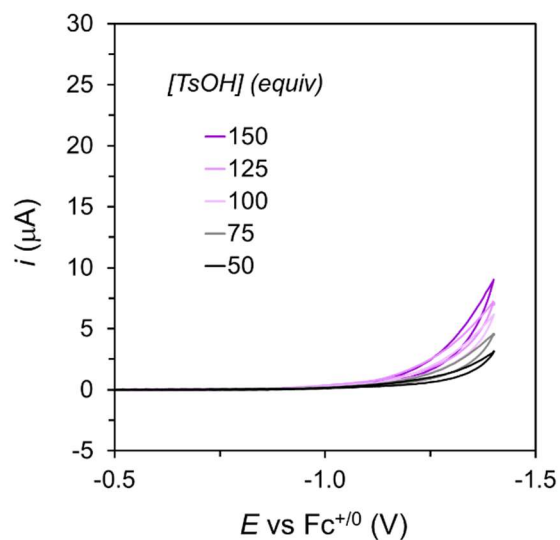


Fig. S61. Background CVs at $100 \text{ mV}\cdot\text{s}^{-1}$ of a 0.1 M $[\text{Li}][\text{NTf}_2]$ THF solution containing increasing concentrations of TsOH, showing an increase in the background HER electrocatalysis mediated by the electrode.

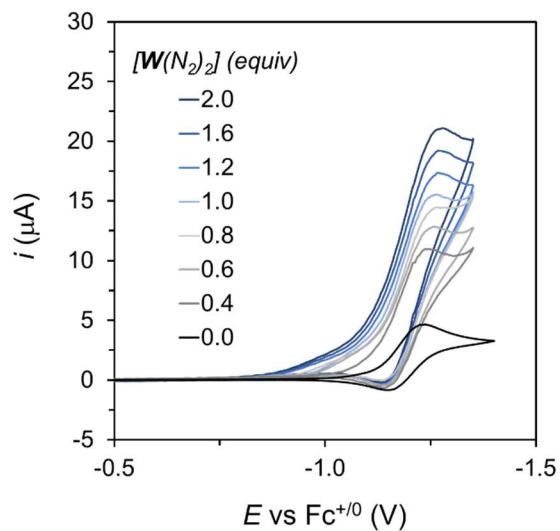


Fig. S62. CVs at $100 \text{ mV}\cdot\text{s}^{-1}$ of a 0.1 M $[\text{Li}][\text{NTf}_2]$ THF solution containing 0.5 mM $\text{Co}(\text{III},\text{N})^+$, 50 mM TsOH and increasing concentrations of $\text{W}(\text{N}_2)_2$, evidencing a partial positive order in $\text{W}(\text{N}_2)_2$ for the electrocatalytic process.

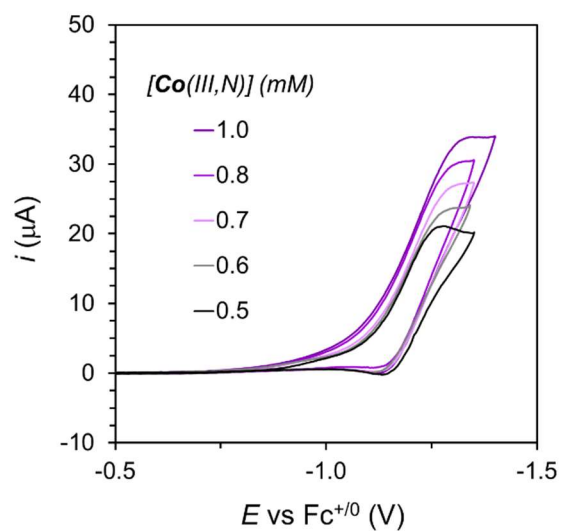


Fig. S63. CVs at $100 \text{ mV} \cdot \text{s}^{-1}$ of a $0.1 \text{ M } [\text{Li}][\text{NTf}_2]$ THF solution containing $0.5 \text{ mM } \text{W}(\text{N}_2)$, 50 mM TsOH and increasing concentrations of Co(III,N)^+ , evidencing a partial positive order in Co(III,N)^+ for the electrocatalytic process.

S9. Electrocatalysis with N₂RR catalysts:

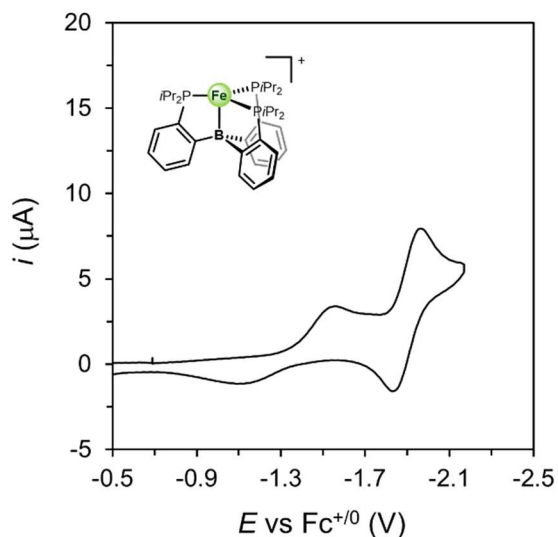


Fig. S64. CV at $100 \text{ mV}\cdot\text{s}^{-1}$ of a $0.1 \text{ M } [\text{Li}][\text{NTf}_2]$ THF solution containing $0.5 \text{ mM } [(\text{TPB})\text{Fe}][\text{BARF}_4]$, showing the subsequent, reversible, one-electron reduction to $\text{Fe}(\text{N}_2)$ (complex **6**) and $\text{Fe}(\text{N}_2)^-$, at around -1.3 V and $-2 \text{ V vs Fc}^{+/0}$, respectively.

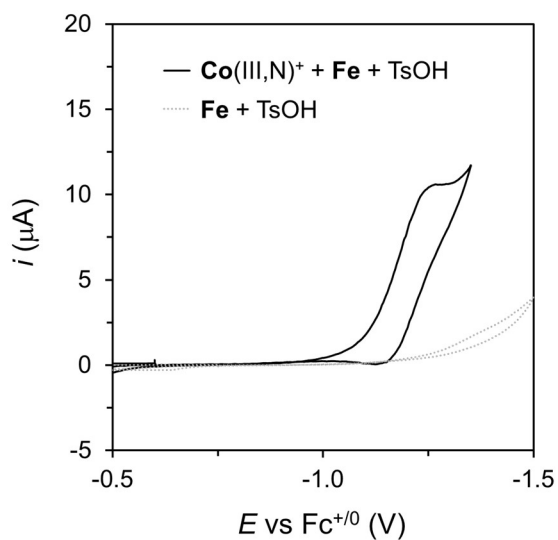


Fig. S65. CV at $100 \text{ mV}\cdot\text{s}^{-1}$ of a $0.1 \text{ M } [\text{Li}][\text{NTf}_2]$ THF solution containing $0.5 \text{ mM } [(\text{TPB})\text{Fe}][\text{BARF}_4]$ and 50 mM TsOH with (black trace) and without (gray trace) $0.5 \text{ mM Co(III,N)}^+$.

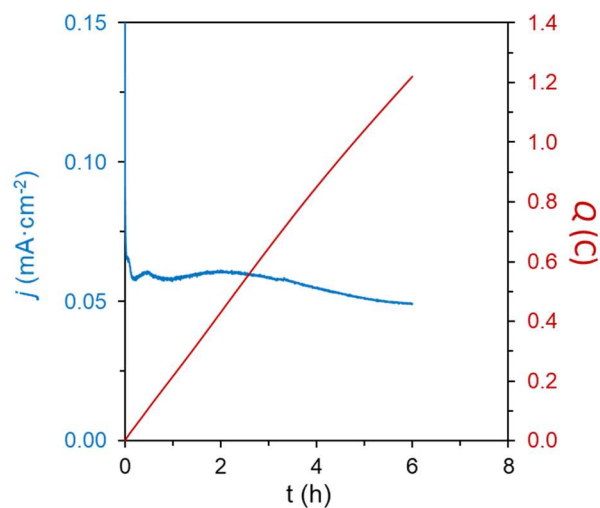


Fig. S66. Current and charge profile for a CPC at -1.35 V vs $\text{Fc}^{+/0}$ in 0.1 M $[\text{Li}][\text{NTf}_2]$ DME solution containing 0.05 mM $\text{Co}(\text{III},\text{N})^+$, 0.05 mM $[(\text{TPB})\text{Fe}][\text{BAr}^{\text{F}_4}]$ and 5 mM TsOH, using a BDD plate working electrode.

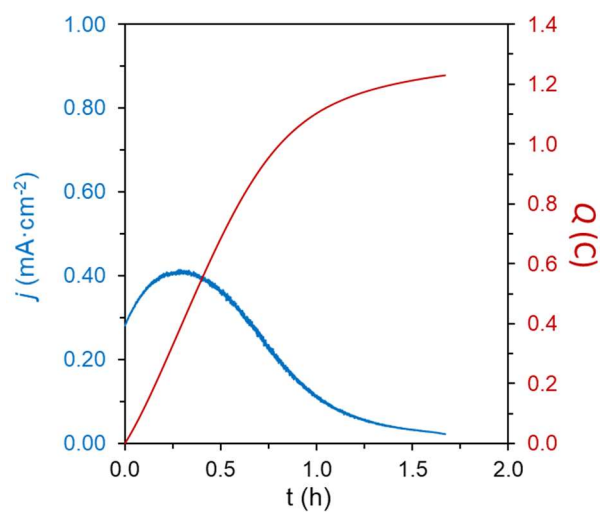


Fig. S67. Current and charge profile for a CPC at -1.45 V vs $\text{Fc}^{+/0}$ in 0.1 M $[\text{Li}][\text{NTf}_2]$ DME solution containing 0.05 mM $\text{Co}(\text{III},\text{N})^+$, 0.05 mM $[(\text{TPB})\text{Fe}][\text{BAr}^{\text{F}_4}]$ and 5 mM TsOH, using a BDD plate working electrode.

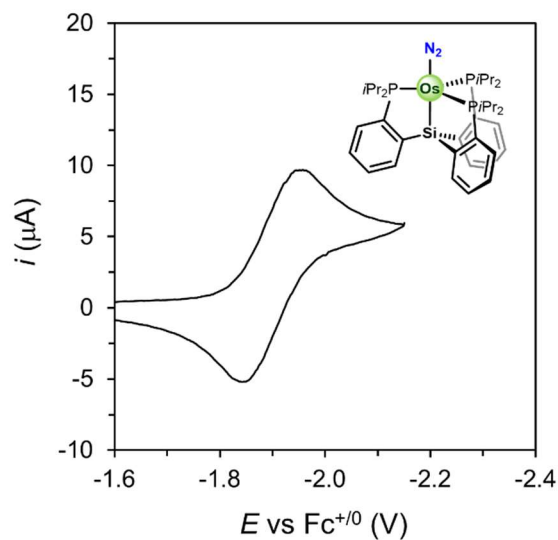


Fig. S68. CV at $100 \text{ mV}\cdot\text{s}^{-1}$ of a 0.1 M $[\text{Li}][\text{NTf}_2]$ THF solution containing 0.5 mM $\text{Os}(\text{N}_2)$ complex **5** showing the reversible, one-electron reduction to $\text{Os}(\text{N}_2)^-$ at around -1.9 V vs $\text{Fc}^{+/0}$.

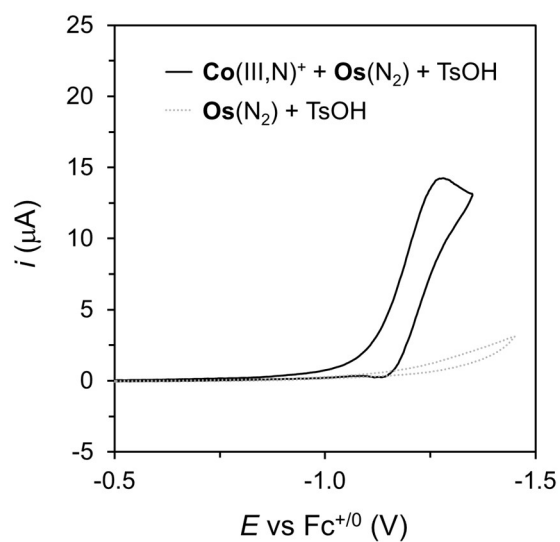


Fig. S69. CV at $100 \text{ mV}\cdot\text{s}^{-1}$ of a 0.1 M $[\text{Li}][\text{NTf}_2]$ THF solution containing 0.5 mM $\text{Os}(\text{N}_2)$ and 50 mM TsOH with (black trace) and without (gray trace) 0.5 mM $\text{Co}(\text{III},\text{N})^+$.

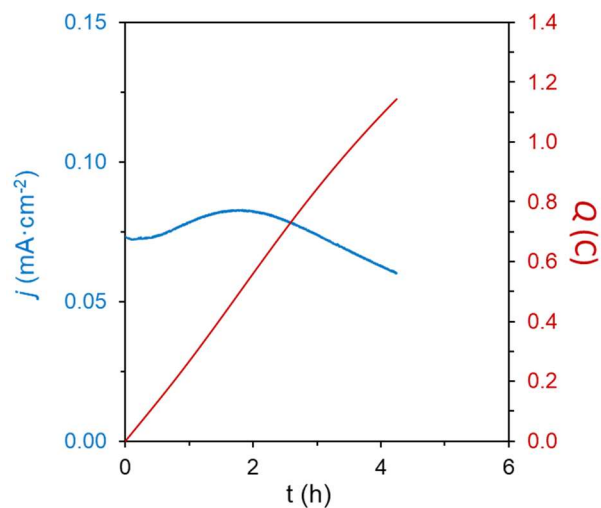


Fig. S70. Current and charge profile for a CPC at -1.35 V vs $\text{Fc}^{+/0}$ in 0.1 M $[\text{Li}][\text{NTf}_2]$ DME solution containing 0.05 mM $\text{Co}(\text{III},\text{N})^+$, 0.05 mM $\text{Os}(\text{N}_2)$ and 5 mM TsOH , using a BDD plate working electrode.

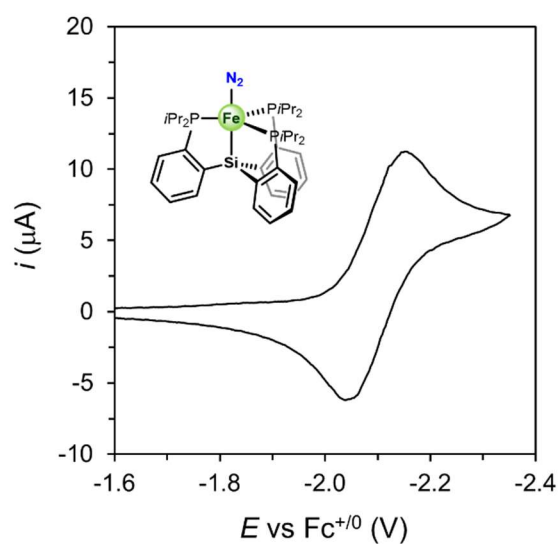


Fig. S71. CV at 100 $\text{mV}\cdot\text{s}^{-1}$ of a 0.1 M $[\text{Li}][\text{NTf}_2]$ THF solution containing 0.5 mM $(\text{SiP}_3)\text{Fe}(\text{N}_2)$ complex **7** showing the reversible, one-electron reduction to $(\text{SiP}_3)\text{Fe}(\text{N}_2)^-$ at around -2.1 V vs $\text{Fc}^{+/0}$.

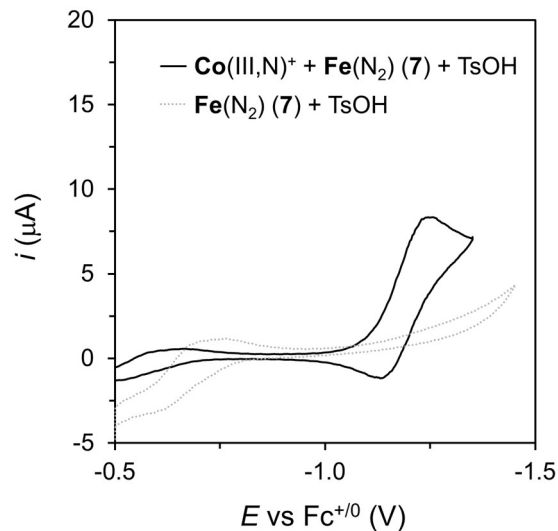


Fig. S72. CV at $100 \text{ mV} \cdot \text{s}^{-1}$ of a 0.1 M $[\text{Li}][\text{NTf}_2]$ THF solution containing 0.5 mM $(\text{SiP}_3)\text{Fe}(\text{N}_2)$ and 50 mM TsOH with (black trace) and without (gray trace) 0.5 mM $\text{Co}(\text{III},\text{N})^+$.

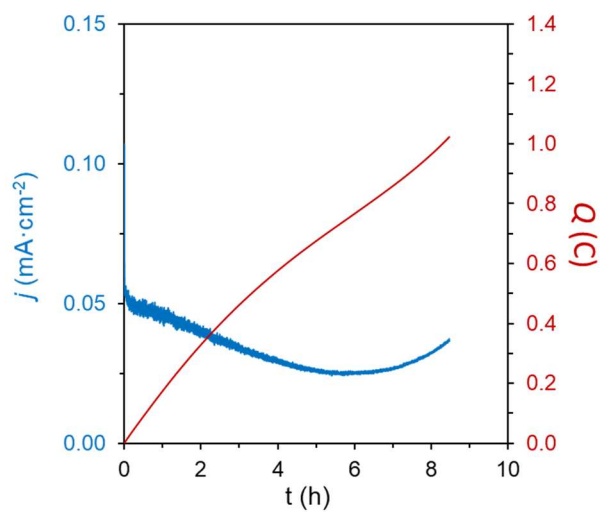


Fig. S73. Current and charge profile for a CPC at -1.35 V vs $\text{Fc}^{+/0}$ in 0.1 M $[\text{Li}][\text{NTf}_2]$ DME solution containing 0.05 mM $\text{Co}(\text{III},\text{N})^+$, 0.05 mM $\text{Fe}(\text{N}_2)$ and 5 mM TsOH, using a BDD plate working electrode.

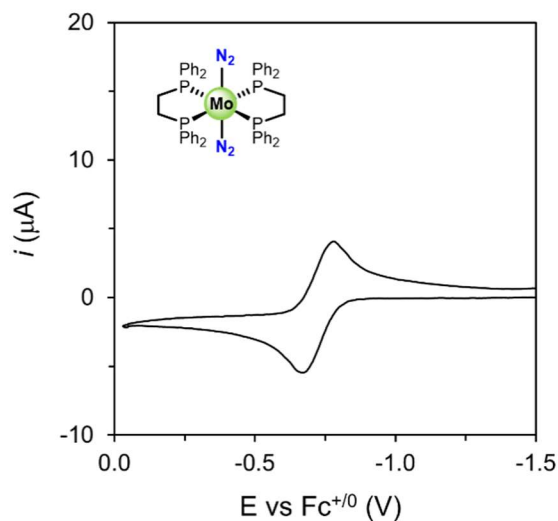


Fig. S74. CV at $100 \text{ mV} \cdot \text{s}^{-1}$ of a 0.1 M $[\text{Li}][\text{NTf}_2]$ THF solution containing 0.5 mM the $\text{Mo}(\text{N}_2)_2$ complex **1** showing a reversible, one-electron redox couple at around -0.7 V vs $\text{Fc}^{+/0}$.

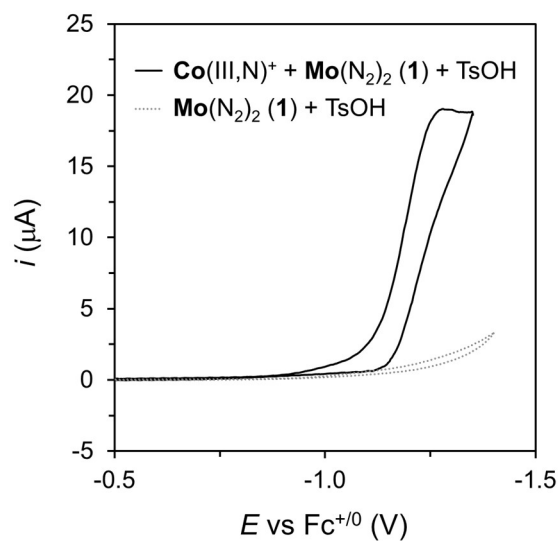


Fig. S75. CV at $100 \text{ mV} \cdot \text{s}^{-1}$ of a 0.1 M $[\text{Li}][\text{NTf}_2]$ THF solution containing 0.5 mM of the $\text{Mo}(\text{N}_2)_2$ complex **1** and 50 mM TsOH with (black trace) and without (gray trace) 0.5 mM $\text{Co}(\text{III},\text{N})^+$.

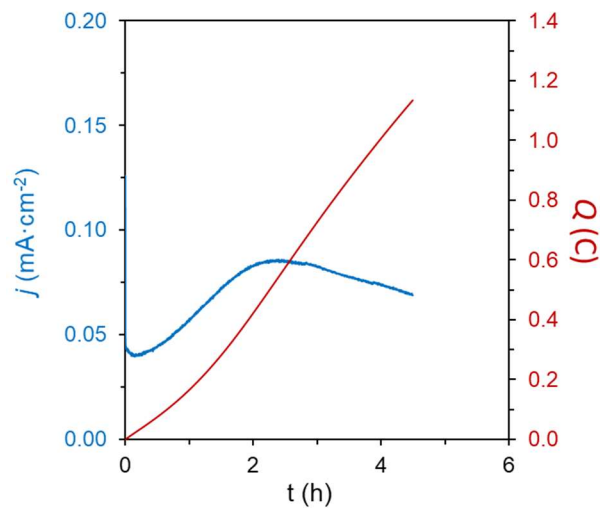


Fig. S76. Current and charge profile for a CPC at -1.35 V vs $\text{Fc}^{+/0}$ in 0.1 M $[\text{Li}][\text{NTf}_2]$ DME solution containing 0.05 mM $\text{Co}(\text{III},\text{N})^+$, 0.05 mM $\text{Mo}(\text{N}_2)_2$ complex **1** and 5 mM TsOH, using a BDD plate working electrode.

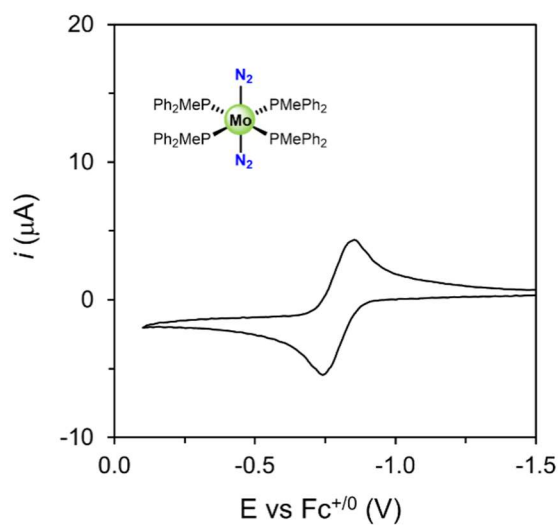


Fig. S77. CV at 100 $\text{mV}\cdot\text{s}^{-1}$ of a 0.1 M $[\text{Li}][\text{NTf}_2]$ THF solution containing 0.5 mM the $\text{Mo}(\text{N}_2)_2$ complex **2** showing a reversible, one-electron redox couple at around -0.6 V vs $\text{Fc}^{+/0}$.

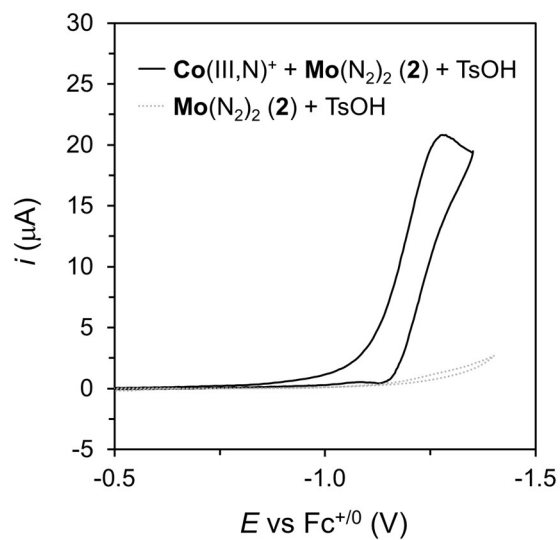


Fig. S78. CV at $100 \text{ mV} \cdot \text{s}^{-1}$ of a 0.1 M $[\text{Li}][\text{NTf}_2]$ THF solution containing 0.5 mM of the $\text{Mo}(\text{N}_2)_2$ complex **2** and 50 mM TsOH with (black trace) and without (gray trace) 0.5 mM $\text{Co}(\text{III},\text{N})^+$.

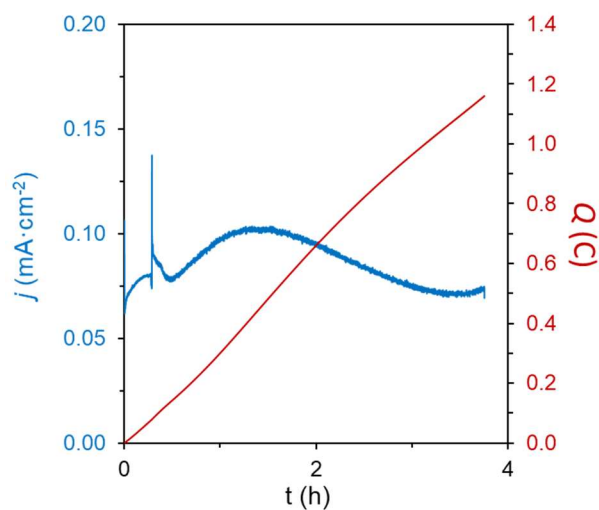


Fig. S79. Current and charge profile for a CPC at -1.35 V vs $\text{Fc}^{+/0}$ in 0.1 M $[\text{Li}][\text{NTf}_2]$ DME solution containing 0.05 mM $\text{Co}(\text{III},\text{N})^+$, 0.05 mM $\text{Mo}(\text{N}_2)_2$ complex **2** and 5 mM TsOH, using a BDD plate working electrode.

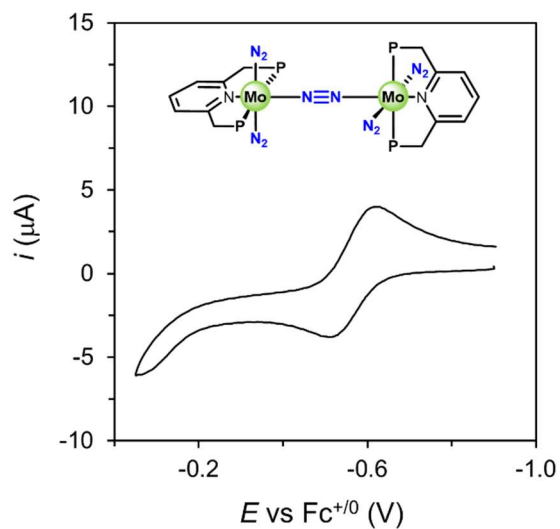


Fig. S80. CV at $100 \text{ mV}\cdot\text{s}^{-1}$ of a 0.1 M $[\text{Li}][\text{NTf}_2]$ THF solution containing 0.5 mM the Mo complex **3** showing a reversible, one-electron redox couple at around -0.6 V vs $\text{Fc}^{+/0}$.

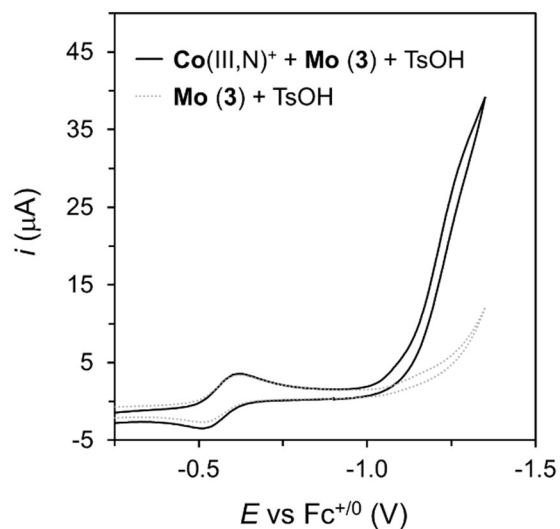


Fig. S81. CV at $100 \text{ mV}\cdot\text{s}^{-1}$ of a 0.1 M $[\text{Li}][\text{NTf}_2]$ THF solution containing 0.5 mM of the Mo complex **3** and 50 mM TsOH with (black trace) and without (gray trace) 0.5 mM $\text{Co}(\text{III},\text{N})^+$.

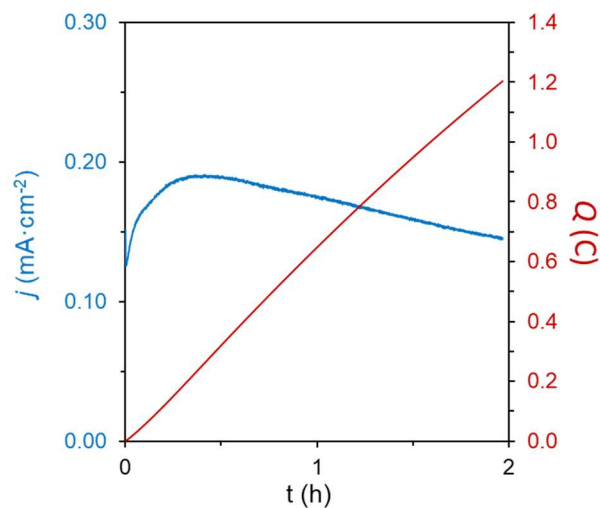


Fig. S82. Current and charge profile for a CPC at -1.35 V vs $\text{Fc}^{+/0}$ in 0.1 M $[\text{Li}][\text{NTf}_2]$ DME solution containing 0.05 mM $\text{Co}(\text{III},\text{N})^+$, 0.05 mM Mo complex **3** and 5 mM TsOH, using a BDD plate working electrode.

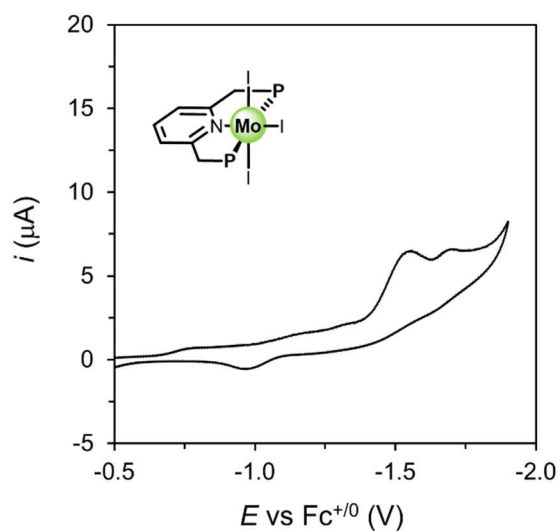


Fig. S83. CV at 100 $\text{mV}\cdot\text{s}^{-1}$ of a 0.1 M $[\text{Li}][\text{NTf}_2]$ THF solution containing 0.5 mM the Mo complex **4** showing two irreversible, one-electron reduction waves below -1.5 V vs $\text{Fc}^{+/0}$.

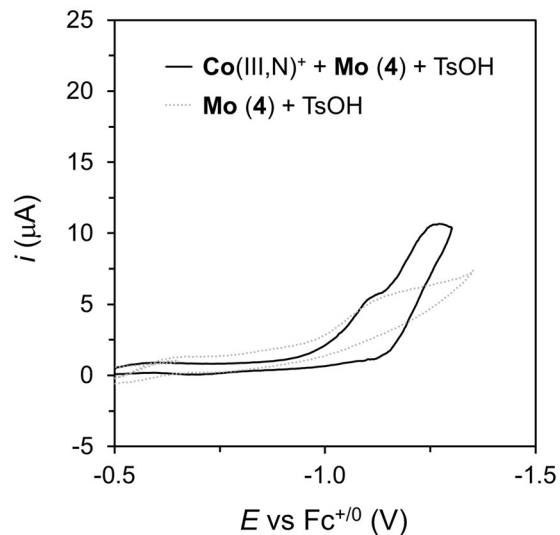


Fig. S84. CV at $100 \text{ mV} \cdot \text{s}^{-1}$ of a $0.1 \text{ M } [\text{Li}][\text{NTf}_2]$ THF solution containing 0.5 mM of the Mo complex **4** and 50 mM TsOH with (black trace) and without (gray trace) $0.5 \text{ mM } \text{Co(III,N)}^+$.

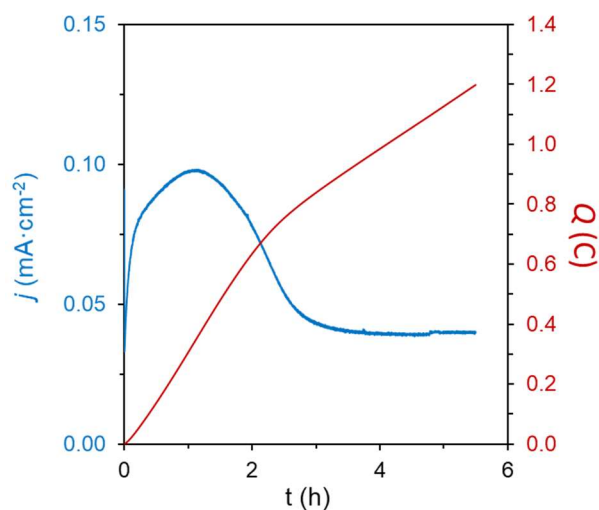


Fig. S85. Current and charge profile for a CPC at $-1.35 \text{ V vs Fc}^{+/0}$ in $0.1 \text{ M } [\text{Li}][\text{NTf}_2]$ DME solution containing $0.05 \text{ mM } \text{Co(III,N)}^+$, 0.05 mM Mo complex **4** and 5 mM TsOH, using a BDD plate working electrode.

S10. References:

- (1) Chalkley, M. J.; Garrido-Barros, P.; Peters, J. C. A Molecular Mediator for Reductive Concerted Proton-Electron Transfers via Electrocatalysis. *Science* **2020**, *369* (6505), 850–854.
- (2) Becker, J. Y.; Avraham (Tsarfaty), S. Nitrogen Fixation: Part III. Electrochemical Reduction of Hydrazido (-NNH₂) Mo and W Complexes. Selective Formation of NH₃ under Mild Conditions. *J. Electroanal. Chem. Interf. Electrochem.* **1990**, *280* (1), 119–127.
- (3) Lane, J. D.; Henderson, R. A. Mechanism of the Reaction between Trans-[W(NNH₂)(p-MeC₆H₄SO₃)(Ph₂PCH₂CH₂PPh₂)₂]⁺ and NEt₃: The Influence of the Metal on the Rates of Proton Transfer of Hydrazido(2-)-Ligands. *J. Chem. Soc., Dalton Trans.* **1987**, No. 1, 197–200.
- (4) Bevan, P. C.; Chatt, J.; Dilworth, J. R.; Henderson, R. A.; Leigh, G. J. The Preparation and Reactions of Azidobis[1,2-Bis(Diphenylphosphino)-Ethane]Nitridotungsten(IV). *J. Chem. Soc., Dalton Trans.* **1982**, *4*, 821–824.
- (5) Ning, Y.; Sarjeant, A. A.; Stern, C. L.; Peterson, T. H.; Nguyen, S. T. One-Pot Synthesis of Mo⁰ Dinitrogen Complexes Possessing Monodentate and Multidentate Phosphine Ligands. *Inorg. Chem.* **2012**, *51* (5), 3051–3058.
- (6) Arashiba, K.; Miyake, Y.; Nishibayashi, Y. A Molybdenum Complex Bearing PNP-Type Pincer Ligands Leads to the Catalytic Reduction of Dinitrogen into Ammonia. *Nat. Chem.* **2010**, *3*, 120–125.
- (7) Ashida, Y.; Arashiba, K.; Nakajima, K.; Nishibayashi, Y. Molybdenum-Catalysed Ammonia Production with Samarium Diiodide and Alcohols or Water. *Nature* **2019**, *568* (7753), 536–540.
- (8) Takaoka, A.; Gerber, L. C. H.; Peters, J. C. Access to Well-Defined Ruthenium(I) and Osmium(I) Metalloradicals. *Angew. Chem. Int. Ed.* **2010**, *49* (24), 4088–4091.
- (9) Anderson, J. S.; Rittle, J.; Peters, J. C. Catalytic Conversion of Nitrogen to Ammonia by an Iron Model Complex. *Nature* **2013**, *501* (7465), 84–87.
- (10) Whited, M. T.; Mankad, N. P.; Lee, Y. H.; Oblad, P. F.; Peters, J. C. Dinitrogen Complexes Supported by Tris(Phosphino)Silyl Ligands. *Inorg. Chem.* **2009**, *48* (6), 2507–2517.
- (11) Del Castillo, T. J.; Thompson, N. B.; Peters, J. C. A Synthetic Single-Site Fe Nitrogenase: High Turnover, Freeze-Quench ⁵⁷Fe Mossbauer Data, and a Hydride Resting State. *J. Am. Chem. Soc.* **2016**, *138* (16), 5341–5350.
- (12) Brown, T. J.; Weber, D.; Gagné, M. R.; Widenhoefer, R. A. Mechanistic Analysis of Gold(I)-Catalyzed Intramolecular Allene Hydroalkoxylation Reveals an Off-Cycle Bis(Gold) Vinyl Species and Reversible C–O Bond Formation. *J. Am. Chem. Soc.* **2012**, *134* (22), 9134–9137.
- (13) Suryanto, B. H. R.; Matuszek, K.; Choi, J.; Hodgetts, R. Y.; Du, H.-L.; Bakker, J. M.; Kang, C. S. M.; Cherepanov, P. V.; Simonov, A. N.; MacFarlane, D. R. Nitrogen Reduction to Ammonia at High Efficiency and Rates Based on a Phosponium Proton Shuttle. *Science* **2021**, *372*, 1187–1191.
- (14) Hodgetts, R. Y.; Kiryutin, A. S.; Nichols, P.; Du, H.-L.; Bakker, J. M.; Macfarlane, D. R.; Simonov, A. N. Refining Universal Procedures for Ammonium Quantification via Rapid

- ¹H NMR Analysis for Dinitrogen Reduction Studies. *ACS Energy Lett.* **2020**, *5* (3), 736–741.
- (15) Macpherson, J. V. A Practical Guide to Using Boron Doped Diamond in Electrochemical Research. *Phys. Chem. Chem. Phys.* **2015**, *17* (5), 2935–2949.
- (16) Costentin, C.; Savéant, J.-M. Multielectron, Multistep Molecular Catalysis of Electrochemical Reactions: Benchmarking of Homogeneous Catalysts. *ChemElectroChem* **2014**, *1* (7), 1226–1236.
- (17) Nielander, A. C.; McEnaney, J. M.; Schwalbe, J. A.; Baker, J. G.; Blair, S. J.; Wang, L.; Pelton, J. G.; Andersen, S. Z.; Enemark-Rasmussen, K.; Čolić, V.; Yang, S.; Bent, S. F.; Cargnello, M.; Kibsgaard, J.; Vesborg, P. C. K.; Chorkendorff, I.; Jaramillo, T. F. A Versatile Method for Ammonia Detection in a Range of Relevant Electrolytes via Direct Nuclear Magnetic Resonance Techniques. *ACS Catal.* **2019**, *9* (7), 5797–5802.
- (18) Kolen, M.; Smith, W. A.; Mulder, F. M. Accelerating ¹H NMR Detection of Aqueous Ammonia. *ACS Omega* **2021**, *6* (8), 5698–5704.
- (19) Pickett, C. J.; Ryder, K. S.; Talarmin, J. Electron-Transfer Reactions in Nitrogen Fixation. Part 2. The Electrosynthesis of Ammonia: Identification and Estimation of Products. *J. Chem. Soc., Dalton Trans.* **1986**, *7*, 1453–1457.
- (20) Al-Salih, T. I.; Pickett, C. J. Electron-Transfer Reactions in Nitrogen Fixation. Part 1. The Electrosynthesis of Dinitrogen, Hydride, Isocyanide, and Carbonyl Complexes of Molybdenum: Intermediates, Mechanisms, and Energetics. *J. Chem. Soc., Dalton Trans.* **1985**, *6*, 1255–1264.
- (21) Geri, J. B.; Shanahan, J. P.; Szymczak, N. K. Testing the Push–Pull Hypothesis: Lewis Acid Augmented N₂ Activation at Iron. *J. Am. Chem. Soc.* **2017**, *139* (16), 5952–5956.
- (22) Bendix, J.; Bøgevig, A. Synthesis and Characterization of a Stable Trans-Dioxo Tungsten(IV) Complex and Series of Mono-Oxo Molybdenum(IV) and Tungsten(IV) Complexes. Structural and Electronic Effects of π -Bonding in Trans-[M(O)(X)(dppe)₂]⁺⁰ Systems. *Inorg. Chem.* **1998**, *37* (23), 5992–6001.
- (23) Xu, K. Nonaqueous Liquid Electrolytes for Lithium-Based Rechargeable Batteries *Chem. Rev.* **2004**, *104*, 10, 4303–4418.
- (24) Lehnert, N.; Tuczek, F. The Reduction Pathway of End-on Coordinated Dinitrogen. I. Vibrational Spectra of Mo/W–N₂, –NNH, and –NNH₂ Complexes and Quantum Chemistry Assisted Normal Coordinate Analysis. *Inorg. Chem.* **1999**, *38* (8), 1659–1670.
- (25) A. Henderson, R. The Mechanism of Formation of Hydrazido(2–)- and Hydrido-Complexes by the Reaction of Dinitrogen Complexes with Acids in Tetrahydrofuran. *J. Chem. Soc., Dalton Trans.* **1982**, *0* (5), 917–925.
- (26) Kireev, N. V.; Filippov, O. A.; Pavlov, A. A.; Epstein, L. M.; Makhaev, V. D.; Dyadchenko, V. P.; Shubina, E. S.; Belkova, N. V. Steric and Acidity Control in Hydrogen Bonding and Proton Transfer to Trans-W(N₂)₂(dppe)₂. *Inorg. Chem.* **2018**, *57* (3), 1656–1664.
- (27) Chatt, J.; Pearman, A. J.; Richards, R. L. Conversion of Dinitrogen in Its Molybdenum and Tungsten Complexes into Ammonia and Possible Relevance to the Nitrogenase Reaction. *J. Chem. Soc., Dalton Trans.* **1977**, *19*, 1852.